

1 **2021 North American Heatwave Amplified by Climate-Change-Driven Nonlinear**  
2 **Interactions**

3

4 Samuel Bartusek<sup>\*,1,2</sup>, Kai Kornhuber<sup>2,3</sup>, Mingfang Ting<sup>2</sup>

5 1. Department of Earth and Environmental Sciences, Columbia University, New York, NY,  
6 USA

7 2. Lamont-Doherty Earth Observatory, Columbia University, Palisades, NY, USA

8 3. Earth Institute, Columbia University, New York, NY, USA

9

10 \*Corresponding author: Samuel Bartusek, [samuel.bartusek@columbia.edu](mailto:samuel.bartusek@columbia.edu)

11

12

13 **Abstract**

14 Heat conditions in North America in summer 2021 exceeded prior heatwaves by margins many  
15 would have considered impossible under current climate conditions. Associated severe impacts  
16 highlight the need for understanding its physical drivers and relations to climate change, to  
17 improve the projection and prediction of future extreme heat risks. Here, we find that slow- and  
18 fast-moving components of the atmospheric circulation interacted, along with regional soil  
19 moisture deficiency, to trigger a 5-sigma heat event. Its severity was amplified ~40% by  
20 nonlinear interactions between its drivers, likely driven by land–atmosphere feedbacks catalyzed  
21 by long-term regional warming and soil drying. Since the 1950s, global warming has  
22 transformed the event’s peak daily regional temperature anomaly from virtually impossible to a  
23 presently-estimated ~200-year occurrence. Its likelihood is projected to increase rapidly with  
24 unmitigated global warming, possibly becoming a 10-yearly occurrence in a climate 2°C warmer  
25 than preindustrial, which may be reached by 2050.

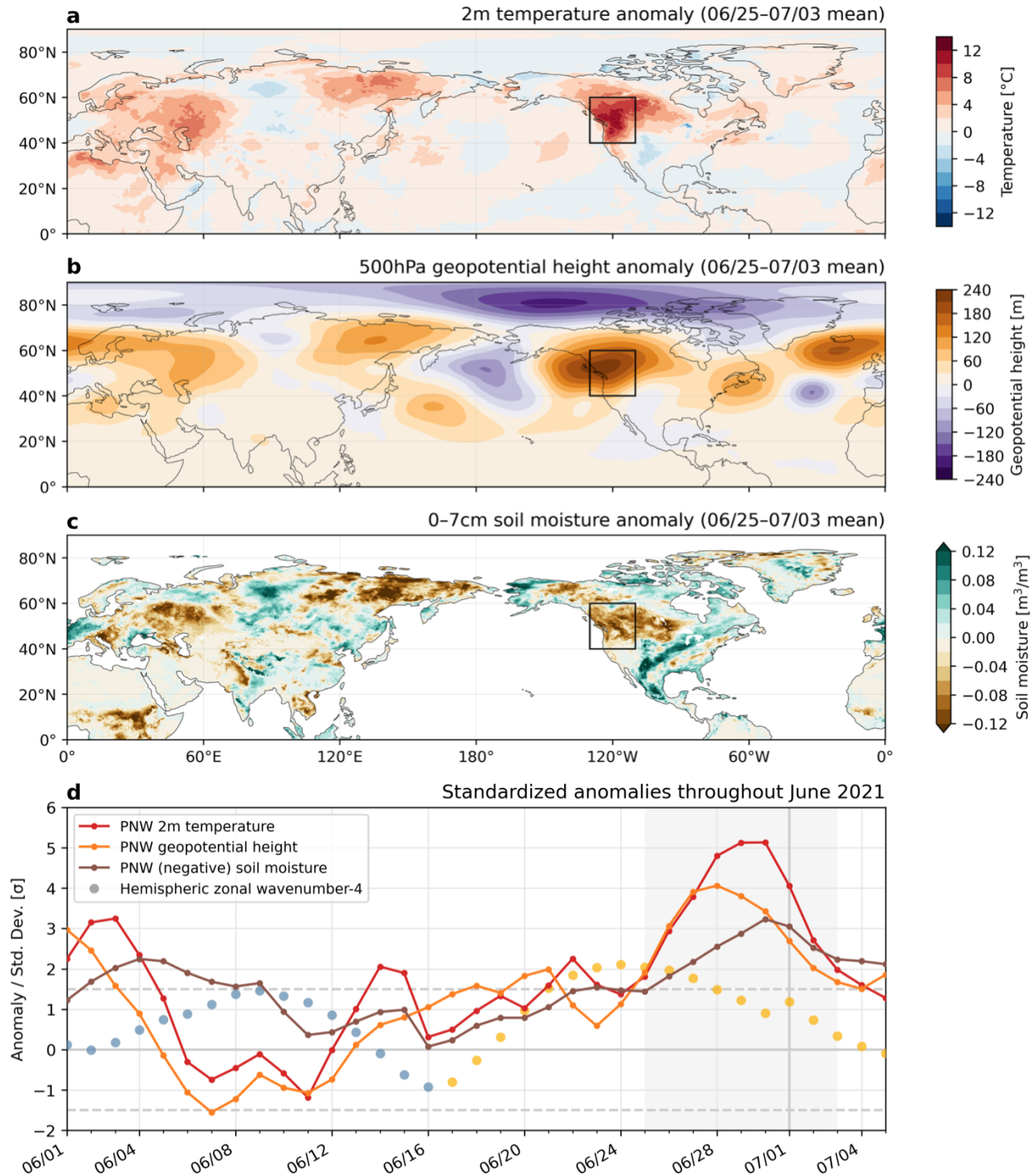
26 **Main**

27 Unprecedented heat conditions in the North American Pacific Northwest (PNW) in late June and  
28 early July 2021 affected millions, likely led to deaths in the thousands, and promoted wildfires  
29 affecting air quality throughout the continent. CDC records suggest hundreds of excess deaths in  
30 both Washington and Oregon during the heatwave, with hundreds more in British Columbia  
31 officially attributed to heat, likely undercounting the true toll<sup>1,2,3</sup>. Heat-related emergency room  
32 visits spiked, totaling nearly 3,000 over June 25–30 in the US PNW<sup>4</sup>. The affected region’s high  
33 vulnerability to extreme heat amplified its dangers: air conditioning access in the Seattle and  
34 Portland metropolitan areas is among the lowest in the country<sup>5</sup>, while many PNW counties have  
35 among the largest outdoor agricultural worker populations and highest social vulnerability in the  
36 country<sup>6</sup>. Exacerbated by drought conditions (covering 95% of the US PNW by June 22<sup>7</sup>),  
37 wildfires sparked during and following the heatwave constituted some of 93 large fires  
38 contributing to millions of western US acres burned by August<sup>8</sup>. Wildfire smoke caused  
39 particulate matter pollution across the continent, for instance contributing to New York City’s  
40 worst air quality in 15 years<sup>9</sup>.

41 Even as global warming increases the severity and frequency of heatwaves<sup>10,11</sup>, the  
42 magnitude of this event exceeded what many may have considered plausible under current  
43 climate conditions<sup>12</sup>. While heat records are typically broken by small increments<sup>13,14</sup>, this event  
44 shattered records by tens of degrees Celsius<sup>15</sup>. Such an unprecedented event raises the pressing  
45 question of whether heat extremes’ future projections are too conservative or their mechanisms  
46 inadequately captured by climate models. It is therefore important to understand the event’s  
47 physical drivers and assess their connections with climate change. From an attribution  
48 perspective, was this anomaly so extreme to be considered virtually impossible regardless of  
49 climate change (a “black swan” event<sup>16,17</sup>), or was it plausible and foreseeable, and even made  
50 more likely due to baseline warming (a “gray swan”<sup>18</sup>)? Further, were its drivers mechanistically  
51 altered by climate trends, beyond their occurrence in a warming background—perhaps indicating  
52 exacerbated future risk?

53 Whether any change in atmospheric dynamics or land–atmosphere interaction is  
54 implicated in amplifying current and future heat extremes is a persistent question: common  
55 heatwave mechanisms may be modified by climate change beyond a shift in background  
56 conditions. Mid-latitude heat extremes, typically triggered by anticyclonic circulation anomalies,

57 have often been associated with persistently-amplified planetary-scale atmospheric waves<sup>19–23</sup>.  
58 Conditions favorable for wave amplification may become more frequent, possibly connected to  
59 weakening of the north-south temperature gradient<sup>24–26</sup>. Additionally, thermodynamic land–  
60 atmosphere feedbacks can strongly amplify heatwave temperatures, often involving nonlinear  
61 processes<sup>27–31</sup>. Land areas typically occupy two distinct regimes of soil–atmosphere interaction:  
62 areas where soil moisture is too high or too low for its variability to affect evapotranspiration,  
63 versus areas with “transitional” climates (between wet and dry), where soil moisture variability  
64 affects evapotranspiration and therefore temperature<sup>32</sup>. The central US is a noted transitional-  
65 climate hotspot of strong soil moisture–temperature coupling<sup>32,33</sup>, but although the presently-wet  
66 PNW is projected to dry due to warming<sup>34–36</sup>, and aridification of other wet regions has been  
67 implicated in amplifying summer temperature variability (e.g. central Europe<sup>37</sup>), the PNW has  
68 not garnered similar focus on land–atmosphere contributions to its temperature variability and  
69 their potential changes.



70 **Fig. 1: Timing and location of the PNW heatwave and its associated atmospheric dynamical**  
 71 **and land-surface conditions. Northern Hemisphere a) Temperature, b) geopotential height, and**  
 72 **c) soil moisture anomalies during the 2021 PNW heatwave (June 25–July 3), and d) their**  
 73 **evolution throughout June averaged over the PNW (black box in a-c); 40–60°N, 110–130°W;**  
 74 **land temperature only). During the heatwave, much of the PNW experienced extreme anomalies**  
 75 **in temperature, geopotential height, and soil moisture exceeding 5, 4, and 3 standard deviations**  
 76 **from their 1981–2010 means. d) also shows the amplitude of a zonal-wavenumber-4 disturbance**

77 *in the midlatitude upper-atmospheric circulation, colored blue when in negative phase and*  
78 *yellow in positive phase (see Methods). This wave corresponds to 4 regions of positive*  
79 *(alternating with 4 negative) geopotential height anomalies encircling the hemisphere, visible in*  
80 *a–c) with associated temperature and soil moisture anomalies affecting the PNW, central*  
81 *Eurasia, and Northeastern Siberia. See Fig. S2 for a detailed perspective on the evolution of*  
82 *atmosphere dynamical aspects.*

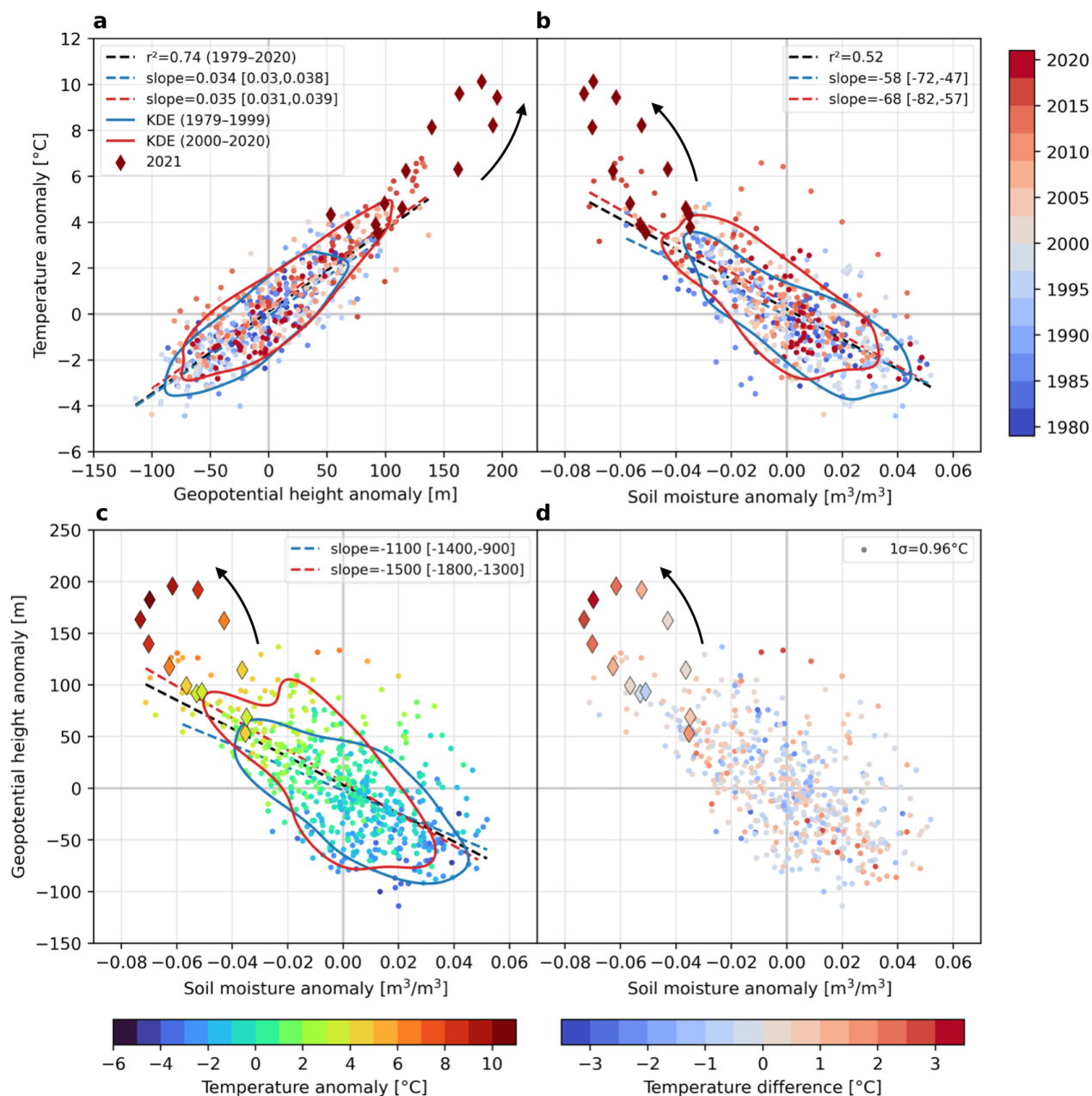
#### 84 **Unprecedented PNW heat conditions and contributing factors**

85 Anomalous near-surface temperatures during the PNW heatwave were accompanied by  
86 extremely high geopotential height and exceptionally low soil moisture. The regionally-averaged  
87 2-meter temperature anomaly over land exceeded 5 times its daily standard deviation over 1981–  
88 2010 (from ERA5 reanalysis; see Methods), while geopotential height and soil dryness  
89 anomalies exceeded 4 and 3 of theirs (Fig. 1d). The PNW experienced at least seven days  
90 exceeding the 99th percentile (1981–2010) in each of these variables (Fig. S1). However, this  
91 analysis of a large region (40–60°N, 130–110°W), capturing the broad-scale meteorological  
92 factors influencing the event rather than focusing on its most severe hotspots, may understate  
93 local severity: in some areas, 9-day-averaged (June 25–July 3) temperature exceeded 12°C above  
94 normal.

95 The PNW was not the only anomalously hot region during this period: a hemisphere-  
96 wide pattern of anomalies extended from the land surface into the mid-atmosphere (Fig. 1a–c).  
97 Central Eurasia and northeastern Siberia both experienced warm anomalies, dry soils and high  
98 geopotential heights; the North Atlantic constituted a fourth high-geopotential-height region.  
99 With alternating cool, wet, and low-height regions, this pattern comprised a circumglobal  
100 wavenumber-4 disturbance (four peaks and troughs in each variable encircling the hemisphere;  
101 see Fig. S2 for further details), a pattern historically associated with North American wildfires<sup>38</sup>.  
102 A wavenumber-4 upper-atmospheric circulation anomaly (see Methods) was established since  
103 June 19 (before the heatwave), and strongly amplified ( $>1.5\sigma$ ) since June 21 (Fig. 1d, Fig. S2).  
104 Accordingly, in late June the jet stream assumed a persistent “wavy” configuration with strong  
105 meridional wind meanders (Figs. S2, S3)—exhibiting a zonal-mean wind and temperature  
106 fingerprint for amplified planetary-scale waves that some evidence suggests may become more  
107 frequent with warming<sup>24,25,39</sup>. Further, convection in the western subtropical Pacific may have  
108 helped excite a late-June Rossby wavetrain extending towards North America that locked phase  
109 with the existing hemispheric wave, amplifying the PNW’s geopotential height and temperature

110 anomalies and perhaps also strengthening the hemispheric wave (Fig. S2), suggesting an  
111 important role for atmospheric dynamics in this event.

112         However, during the heatwave the PNW experienced markedly stronger temperature and  
113 height anomalies than other nodes of the hemispheric wave, despite similar soil moisture  
114 anomalies (compare Fig. 1b and 1c). Additionally, regional temperature continued rising during  
115 the event after geopotential height had peaked, mirroring the direction of soil moisture anomalies  
116 (Fig. 1d, Fig. S1). These observations suggest a potential role for both shorter-term atmospheric  
117 dynamics and two-way land–atmosphere feedbacks in amplifying and prolonging the PNW  
118 heatwave.



119 **Fig. 2: Nonlinear interactions of common drivers and their long-term trends.** a): 3-day  
 120 running means of PNW-mean 2m temperature versus 500hPa geopotential height anomalies,  
 121 centered on each day from June 23–July 5 (maximizing on June 30), colored by year (1979–  
 122 2020). Dark red diamonds show 2021 values; the arrow indicates their temporal evolution and  
 123 the historical linear regression between the variables in black. Red and blue dashed lines show  
 124 regressions over 1979–1999 and 2000–2020 with 95% confidence intervals provided in legends.  
 125 Red and blue curves illustrate the 0.5 contour of a KDE of the variables’ 2-dimensional  
 126 distribution for each of the periods. b–c): same as a) for soil moisture versus temperature  
 127 anomalies and versus geopotential height anomalies; markers in c) colored by temperature  
 128 anomaly. d): same as c) but dots colored by the difference between the observed (colors in c))  
 129 and predicted temperature for each soil moisture and geopotential height value pair (by multiple

130 *linear regression; see Fig. S4), indicating that the event's highest temperatures involved*  
131 *nonlinear contributions of  $\sim 3^{\circ}\text{C}$  out of a total  $\sim 10^{\circ}\text{C}$  anomaly.*  
132

### 133 **Nonlinear heat contributions from land–atmosphere interactions**

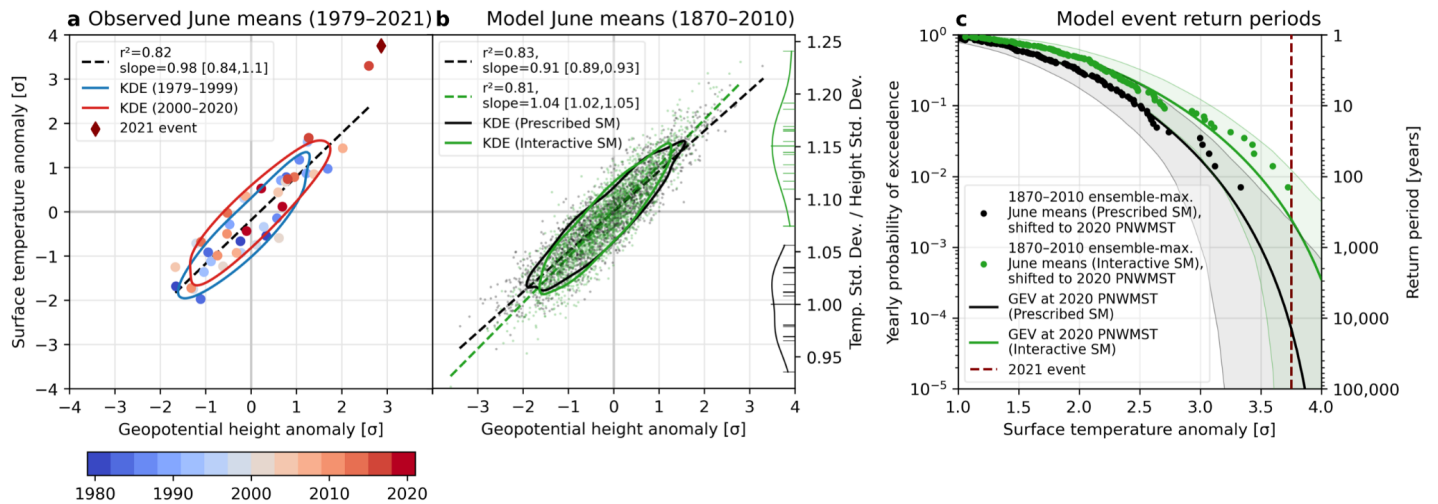
134 Interactions in the land–atmosphere system likely intensified the heatwave, contributing to a  
135  $\sim 3^{\circ}\text{C}$  nonlinear component (of the total  $\sim 10^{\circ}\text{C}$  peak regional-mean heat anomaly) above the heat  
136 accounted for by linear processes (Fig. 2). The heatwave's proximate causes were extreme  
137 anomalies in common heatwave drivers—high geopotential height (resulting from wave-wave  
138 interaction; Fig. S2), and dry soil, which both exceeded their historical (1979–2020) ranges yet  
139 largely followed expected bivariate distribution relationships (Fig. 2a–c), as in simulated record-  
140 shattering heatwaves in similar regions<sup>15</sup>. However, the heatwave's peak temperatures markedly  
141 exceeded temperature's linear regressions against geopotential height or soil moisture (by 4–  
142  $5^{\circ}\text{C}$ ), which are otherwise strongly predictive (Fig. 2a–b). A multiple regression, incorporating  
143 their simultaneous anomalies, confirms nonlinear temperature amplification maximizing during  
144 the event's peak at  $\sim 3^{\circ}\text{C}$  (i.e., increasing  $\sim 7^{\circ}\text{C}$  by  $\sim 40\%$ ), a  $\sim 3\sigma$  amplification (Fig. 2c–d). Two-  
145 way soil moisture–temperature interactions likely drove these nonlinearities, since the  
146 amplification term increased as soils continued to dry, despite geopotential height stagnating and  
147 declining (Fig. 2d, Fig. 1d). That the amplification term behaved out-of-phase with geopotential  
148 height but in-phase with soil moisture is clearer in daily-mean data (Fig. S5), revealing that the  
149 day with strongest nonlinear amplification coincided with the driest soil moisture anomaly (and  
150 highest temperature anomaly), but occurred three days after the geopotential height anomaly  
151 peaked.

152 From a spatial perspective, dryness across much of the region from a beginning-June  
153 heatwave persisted throughout June, even during cool periods, establishing potential  
154 preconditions for land-atmosphere feedbacks (Fig. S6; Fig. 1d). Low evaporative fraction  
155 anomalies collocated with many of the event's highest temperature anomalies (primarily non-  
156 mountainous interior areas with semi-arid and Mediterranean climates; Fig. S7), further  
157 suggesting feedbacks' importance—meanwhile, many such areas have experienced multidecadal  
158 summer drying, warming, and temperature variability increases (Figs. S7, S8; see Conclusions).  
159 Additionally, since upwind drought can enhance heatwaves via advection<sup>40</sup>, dry anomalies east  
160 of the PNW (Fig. 1c) may have also provided amplification via strong easterlies (Fig. 1d; Fig.  
161 S9). An investigation of the 850hPa-level temperature budget during this event substantiates that



162 land-atmosphere processes likely amplified the heating, especially where and when it was  
163 strongest (Fig. S9), though further analysis is needed to link 850hPa-level behavior directly to  
164 surface processes.

165 Furthermore, ongoing regional trends favor the nonlinear behavior amplifying the  
166 heatwave—thus while 2021’s extreme heat was unprecedented, it was nevertheless  
167 mechanistically linked to local climate change. First, the driver variables’ distributions have  
168 individually shifted towards 2021’s conditions: late-June–early-July temperature, geopotential  
169 height, and soil dryness increased over 1979–2020, with trends accelerating over 1991–2020  
170 (Fig. S10, 11). Consequently, these variables’ largest historical extremes tend to occupy more  
171 recent years (Fig. 2a–b). Second, bivariate distributions combining these variables have shifted  
172 towards high temperature and geopotential height and dry soils occurring simultaneously (Fig.  
173 2a–b, visually comparing KDE contours). Notably, historical extreme temperatures approaching  
174 2021 conditions have also tended to be displaced above the linear driver regressions (Fig. 2a–b).  
175 Indeed, while bivariate distribution shifts have primarily followed their underlying regressions,  
176 the slopes describing the temperature and geopotential height relationships with soil moisture  
177 have strengthened (with probability 71% and 98%, respectively, via bootstrapping), indicating  
178 magnified temperature and geopotential height anomalies relative to soil moisture anomalies  
179 (Fig. 2b–c). Temperature–height density contours also potentially suggest a changing  
180 relationship in the distribution’s positive extremes, despite the unchanging linear relation (Fig.  
181 2a), suggesting a change specific to heatwave mechanisms. While these conclusions hold over all  
182 of June–July (Fig. S5), we note that late-June–early-July has exhibited especially pronounced  
183 trends in these variables and their variabilities (Fig. S11), perhaps reflecting advancing summer  
184 onset<sup>41</sup>.



185 **Fig. 3: Modeled PNW monthly temperature variability and extreme event return periods, with**  
 186 **versus without soil moisture interaction. June-mean PNW-mean surface temperature versus**  
 187 **500hPa geopotential height anomalies (standardized), from a) reanalysis (1979–2021) and b)**  
 188 **the CAM5–GOGA model experiment (1870–2010), comparing Prescribed (black) versus**  
 189 **Interactive (green) soil moisture ensembles. Regressions and KDE contours (with 1.25x**  
 190 **smoothing in a) and showing the 0.3 contour in b)) are as in Fig. 3. b) also compares (right y-**  
 191 **axis) the ratio of each member’s geopotential height standard deviation to the Prescribed**  
 192 **ensemble-total temperature standard deviation. Longer lines show ensemble-total ratios; curves**  
 193 **show KDEs. c) shows exceedance probability and return period as a function of standardized**  
 194 **temperature anomaly for GEV distributions (curves) fit to 1870–2010 ensemble-maximum June**  
 195 **means and empirical return periods (dots). The June 2021 temperature anomaly ( $\sim 3.75\sigma$ ) is  $\sim 35$ -**  
 196 **fold more likely ( $\sim 400$ -yr vs.  $\sim 14,000$ -yr return period) with interactive soil moisture.**  
 197

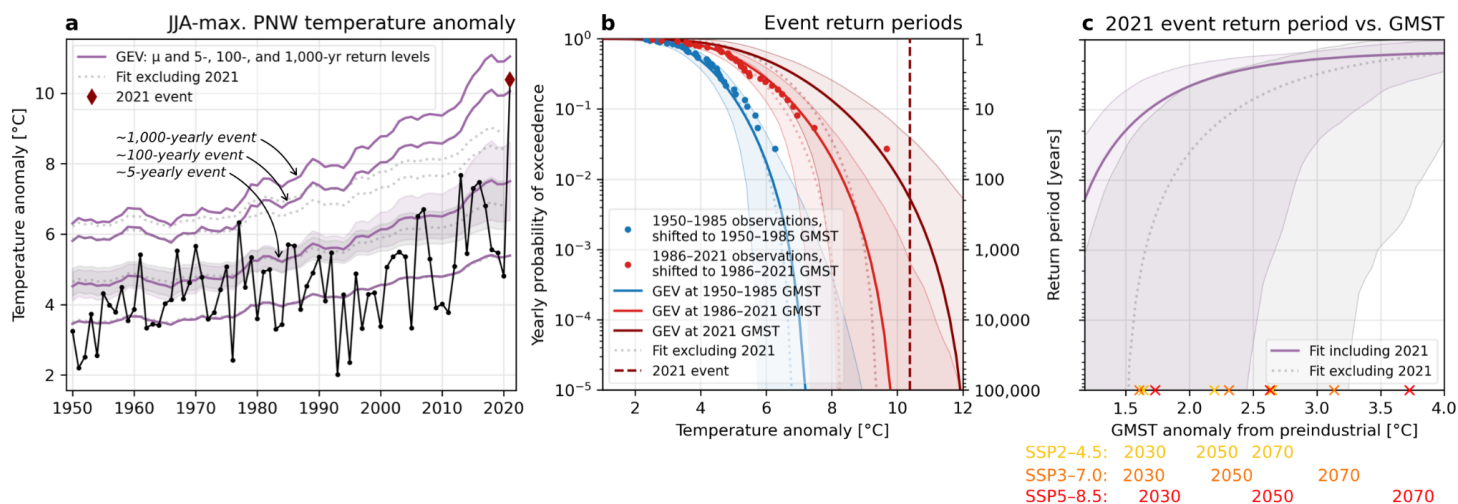
### 198 Role of soil moisture in amplifying PNW temperature extremes

199 Using a model experiment tailored to evaluate the role of soil moisture in climate, we determine  
 200 that in the PNW, soil moisture–atmosphere interactions likely make monthly-scale temperature  
 201 extremes of June 2021’s magnitude many times more probable. We force a climate model with  
 202 historical (1870–2010) sea surface temperatures, both with and without soil moisture  
 203 interactivity (hereafter, Interactive and Prescribed ensembles), and we compare June-mean  
 204 surface temperature model output with observations (2-meter temperature was not available). We  
 205 first confirm that the observed June-mean 2021 surface temperature was extreme (Fig. 4a), with  
 206 monthly temperature reaching  $\sim 3.75\sigma$  and exceeding its regression against geopotential height.  
 207 In the model (standardized for comparison with observations; see Methods), we find that soil  
 208 moisture interaction significantly increases the ratio of monthly temperature variability versus  
 209 geopotential height variability between ensembles in total (by 15%), and across all members

210 individually (Fig. 4b, right axis). Consistent with previous research<sup>42</sup>, temperature variability  
211 increases modestly in Interactive members, accompanying strongly increased mean temperature  
212 (Fig. S12). Accordingly, the height–temperature regression slope across all member-months is  
213 significantly steeper in Interactive (by 14%), while both lie within the confidence interval of the  
214 observed slope (Fig. 4b, left axis). However, this linear slope increase may underestimate  
215 changes toward the distributions’ tails, i.e. during extremes (Fig. 4b, KDE contours).

216         Consequently, the likelihood of June 2021’s standardized temperature anomaly  
217 significantly increases when soil moisture interacts with the atmosphere. Generalized Extreme  
218 Value (GEV) distributions are fit to each ensemble’s yearly ensemble-maximum June-mean  
219 temperature anomaly (see Methods), and their location parameters are nonstationary in 5-year-  
220 smoothed annual PNW-mean surface temperature (PNWMST). We use PNWMST as a covariate  
221 to account for differing PNW mean climate responses to global temperature between model  
222 configurations. Estimated empirical return periods are overlaid on the model curves, with each  
223 observation shifted by the GEVs’ location parameter dependence on PNWMST. Fits and  
224 observations for each ensemble can thus be compared at a consistent baseline: at 2020’s  
225 PNWMST the GEV models estimate a ~35-fold increase (95% CI: 0.07–700,000) in the  
226 likelihood of 2021’s observed monthly anomaly between Prescribed and Interactive SM  
227 ensembles, transforming from an extremely unlikely ~15,000-year (440–∞) event to a ~410-year  
228 (80–∞) event. Overlaid empirical return periods suggest that GEV-derived return periods may  
229 conservatively estimate particularly severe events. Qualitatively similar results are found if two-  
230 or three-year GEV block sizes are used, or if all JJA months are used instead of just June (not  
231 shown).

232



233  
 234 **Fig. 4: 2021 heatwave likelihood estimates over recent decades and under future emissions**  
 235 **pathways. a):** A GEV distribution fit to yearly June–August (JJA)-maximum daily-mean PNW-  
 236 mean 2m temperature overlaid on observations, both including (purple) and excluding (gray  
 237 dotted) 2021’s event, plotting the location parameter ( $\mu$ ) and 5-, 100-, and 1000-year return  
 238 period temperature levels (5-year return level bootstrapped 95% confidence interval shaded). **b):**  
 239 return periods of temperature anomalies for historical periods 1950–1985 and 1986–2021 (fits  
 240 are evaluated at and observations are shifted to the period-mean GMSTs), and estimating a  
 241 ~200-yr return period by 2021. **c):** GEV fits evaluated as a function of GMST, providing  
 242 likelihood estimates for a future analogous event under different emission pathways (CMIP6  
 243 multimodel-mean warming trajectories are displayed for reference). Future probabilities far  
 244 exceed those estimated until today: the event may become a 10-year event before 2050 in even an  
 245 intermediate emissions scenario (SSP2-4.5).

246  
 247 **Increasing event likelihood driven by climate change**

248 Recent climate change has rapidly increased the likelihood of the 2021 heatwave: over the past  
 249 70 years, such an event has multiplied in probability from virtually impossible to a multi-  
 250 hundred-year event (Fig. 5). As above, we apply GEV analysis, a targeted approach for  
 251 estimating extreme value statistics and an established method for attributing climate extremes to  
 252 anthropogenic warming<sup>43–45</sup>. We note, however, that assessing the probability of this event in  
 253 temperature alone—despite its multivariate extreme characteristics—likely conservatively  
 254 estimates its increasing likelihood as a compound event, given simultaneous trends in other  
 255 variables such as soil moisture.

256 First, we find that the PNW has experienced not only shifting mean temperatures but also  
 257 changing variability since 1979: daily-mean June–July temperature anomalies have displayed  
 258 positive and increasing skewness both regionally-averaged (Fig. S14) and across many within-

259 region areas (Fig. S8). While station-based daily-maximum and -minimum temperatures during  
260 July–August have shown small skewness in the PNW and not displayed strong historical  
261 increases<sup>46</sup>, here we highlight an earlier summer period and daily-mean temperatures. We further  
262 note that research has projected future modeled temperature skewness increases under CO<sub>2</sub>  
263 forcing in the PNW, likely linked to soil moisture interaction<sup>47</sup>.

264 We apply GEV analysis to yearly-maximum June–August (JJA) daily temperatures  
265 extending back to 1950, to maximize sample size and robustness, with both location and scale  
266 parameters nonstationary in 5-year-smoothed global mean surface temperature (GMST; see  
267 Methods; stationary scale parameter results are shown in Fig. S15). Results reveal drastic  
268 historical changes in heatwave probabilities: a hypothetical daily 8°C regional temperature  
269 anomaly is estimated to have been virtually impossible in the 1950–1985 climate, but has  
270 become a ~50-year event in the climate since 1986 (Fig. 5b). Similarly, the 2021 heatwave (a  
271 ~10.4°C peak anomaly, far exceeding the historical range) was virtually impossible even at the  
272 average global temperature over 1986–2021 (return period 95% CI: 1,500–∞), but by 2021 has  
273 become a ~200-year event (25–∞)—thereby experiencing an infinite increase in probability (at  
274 least ~13-fold). Its probability increase since 1950–1985 is likewise infinite (at least ~500,000-  
275 fold). Furthermore, the probability of an event exceeding 2021’s magnitude will increase rapidly  
276 under further-increasing GMST—projected to recur ~10-yearly before 2050 even at the warming  
277 of SSP2-4.5, a ‘moderate’ emissions scenario (before 2070 if excluding 2021 from the fit; Fig.  
278 5c).

279 Fig. 5 shows GEV fits both including 2021’s heatwave as well as excluding it. In  
280 including 2021, we follow Van Oldenborgh et al.<sup>44</sup> and Philip et al.<sup>45,48</sup>, assuming 2021’s  
281 observation is drawn from the same distribution as historical observations, since the study region  
282 was not selected solely to maximize local extremity but rather for a large-scale regional  
283 perspective, reducing (but not eliminating) selection bias. The excluding-2021 fit estimates a  
284 finite maximum possible temperature well below the 2021 observation even under current  
285 warming (Fig. 5b), questioning its validity. We note that the including-2021 fit is not rejected by  
286 a Kolmogorov-Smirnov test (Fig. S13) despite its poor fit in similar analyses<sup>48</sup>, which  
287 maintained a fixed scale parameter and analyzed a smaller region more concentrated on the  
288 extreme. Ultimately, both fits underscore dramatic increases in heat extreme probabilities  
289 resulting from gradual warming: in both, a ~1,000-year event in the 1950s would currently

290 resemble a ~5-year event, and has been surpassed multiple times (Fig. 5a). Furthermore,  
291 comparing future projections of a 2021-magnitude event, the fits roughly converge, both  
292 projecting <10-yearly recurrences by 2.5°C GMST above preindustrial. This threshold only  
293 increases to 2.75°C GMST in a fit with stationary instead of nonstationary scale parameter (Fig.  
294 S15).

295

296

297

298

**299 Conclusions**

300 Given the 2021 heatwave's extreme magnitude, an important question is whether it represents a  
301 black swan event<sup>16,17</sup>, effectively unforeseeable no matter the climate conditions; a gray swan  
302 event<sup>18</sup>, made plausible by linking to common drivers and even more likely by background  
303 warming; or further, an event whose drivers do not act stationarily with respect to a moving  
304 background climate but are instead mechanistically altered by climate trends—with event  
305 likelihood thereby increasing beyond that induced by a background shift. We first find that,  
306 although 2021's event was unprecedented by large margins, it was traceable to common drivers,  
307 exhibiting extreme anomalies<sup>15</sup>. Interacting circulation features provided highly anomalous  
308 atmospheric dynamical forcing ( $4\sigma$  geopotential height exceedance), and land–atmosphere  
309 feedbacks likely amplified the event's severity, contributing to a ~40% nonlinear amplification.  
310 Further, however, we also find that the interactions amplifying this heatwave are mechanistically  
311 linked to ongoing regional trends in temperature, soil moisture, and geopotential height  
312 increasing their likelihood, possibly suggesting a shift in feedback behavior underway in the  
313 region compounding background warming.

314 In contrast to first assessments<sup>48</sup> who concluded that the atmosphere dynamical patterns  
315 during this extreme were likely not exceptional, we provide evidence that the interaction of a  
316 persistent anomalous wavenumber-4 Rossby wave in the polar front jet and an atmospheric wave  
317 emanating from the Pacific likely played a key role in this extraordinary temperature anomaly  
318 (Fig. 1, Fig. S2). Further research is required to assess if the conditions for such waves are  
319 becoming more likely, e.g. by strengthened waveguidability<sup>49</sup> of the polar front jet due to  
320 amplified land warming at high latitudes<sup>50,51</sup> or increased convective activity in the tropical  
321 Pacific.

322 Warming-forced midlatitude land drying<sup>34,35</sup> could shift wet regions, such as much of the  
323 PNW, towards a transitional climate between wet and dry, possibly strengthening land-  
324 atmosphere feedbacks and temperature variability<sup>32</sup>. However, the PNW has received little  
325 examination of shifting soil moisture–temperature coupling, despite that some PNW areas  
326 already occupy transitional regimes during summer<sup>52,53</sup> and dry soil–heatwave linkages in the  
327 region are recognized<sup>54</sup>. Our findings suggest that rapid soil drying (particularly in early July,  
328 drying ~7% regionally between 1979–1999 and 2000–2020; Fig. S11) may already be altering  
329 extreme heat mechanisms: many of the 2021 heatwave's anomalously hottest temperatures

330 occurred in areas experiencing long-term decreasing evaporative fraction and increasing  
331 temperature variability (Fig. S7, 8). Additionally, we find increasing trends in four metrics of the  
332 terrestrial component of land–atmosphere coupling in many of the same areas since 1979 (Fig.  
333 S8). Notably, land-atmosphere coupling and temperature variability increases are strongest  
334 where soil moisture is climatologically moderate instead of the driest areas—thus in the PNW,  
335 drying may increase temperature variability more than in already-arid regions like the  
336 southwestern US<sup>32</sup>. In accordance with recent research demonstrating the emergence of heat-  
337 amplifying land–atmosphere feedbacks in regions not historically experiencing them<sup>31</sup> and,  
338 moreover, projections of widespread midcentury soil moisture regime shifts including the  
339 PNW<sup>36</sup>, we suggest that the 2021 heatwave may represent an alarming manifestation of a shifting  
340 regime across much of the PNW from wet to transitional climate, making such events more  
341 likely through strengthened soil moisture–temperature coupling—however, further research is  
342 required to substantiate this.

343         Our results underscore that even gradual warming over recent decades dramatically  
344 transformed the character of this event. Since 1950, an anomaly of this magnitude has been  
345 refigured from virtually impossible to plausible and somewhat expected, with a hundreds-of-  
346 years return period. Continued warming will cause the probability of an equal or stronger event  
347 to rapidly increase, potentially becoming a ~10-year occurrence with 2°C warming above  
348 preindustrial, potentially reached by 2050 in even a ‘moderate’ emissions scenario.

349



350 **Methods**

351

352 **Reanalysis data**

353 All reanalysis data are provided by ECMWF's ERA5<sup>55</sup>, obtained at  $\sim 0.25^\circ$  and 6-hourly  
354 resolution; all analyses involve daily or longer means.

355

356 **Model data**

357 The model experiment we present in Fig. 3b–c is referred to as CAM5–GOGA<sup>56,57</sup>. The  
358 atmospheric model is CAM5 (National Center for Atmospheric Research [NCAR] Community  
359 Atmosphere Model, version 5.3), which is the atmospheric component of the Community Earth  
360 System Model, version 1.2<sup>58</sup>, at T42 spectral ( $\sim 2.75^\circ$ ) resolution. The GOGA (Global Ocean  
361 Global Atmosphere) experiment involves forcing 16 members of CAM5 with historical monthly  
362 sea surface temperatures (HadISSTv2<sup>59</sup>) over the period 1856–2014. Greenhouse gasses (GHGs)  
363 and radiative forcing are fixed (GHGs at 2000 levels), and sea ice concentration follows  
364 HadISSTv2. One 16-member ensemble allows soil moisture to interact with the atmospheric  
365 model, while the other prescribes soil moisture as the monthly climatology over 1950–2015 at  
366 each location derived from all members. We begin analysis in 1870 to avoid model spin-up  
367 effects, and discard two full members and all years after 2010 due to data discrepancies, resulting  
368 in a 14-member by two-ensemble by 141-year dataset. For comparison with reanalysis, we  
369 standardize all anomalies, based on the whole period for all grouped Prescribed members, for  
370 model data, and based on the 1981–2010 climatology for reanalysis data. We note a caveat that  
371 in this experimental design, water is not strictly conserved in the Prescribed SM case, as noted  
372 for GLACE-CMIP5 models<sup>42,60,61</sup>—however, an analysis of the resulting water balance  
373 perturbation in the CESM model<sup>60</sup> shows the perturbation is small in the PNW relative to other  
374 global regions.

375 Future GMST trajectories in Fig. 4c are based on decadal-mean CMIP6 multimodel mean  
376 anomalies from the preindustrial period (1850–1900), using all models available (42 for SSP2-  
377 4.5, 35 for SSP3-7.0, and 44 for SSP5-8.5<sup>62</sup>).

378

379 **Planetary wave analysis**

380 We apply a Fourier transform to 15-day running means of 300hPa meridional wind averaged  
381 over 37.5–52.5°N, obtaining amplitudes and phase positions of the circulation components of  
382 zonal wavenumbers  $k=1-9$ . Amplitudes are compared with a monthly climatology over 1981–  
383 2010 to calculate standardized anomalies.

384

### 385 **Extreme value analysis**

386 Our estimates of likelihoods and return periods of extreme temperatures are derived by fitting  
387 Generalized Extreme Value (GEV) distributions to both observational (ERA5) and model data,  
388 following widely-used procedures designed for investigating extreme events rather than the body  
389 of distributions<sup>43–45,48,63</sup>. For all GEV analysis we use the Python package *climextRemes*<sup>64</sup>.

390 For observations, we first calculate the maximum daily-mean PNW-mean temperature  
391 anomaly over June–August (JJA) each year since 1950 using the ERA5 back extension<sup>65</sup>. We fit  
392 a GEV function with nonstationary location and scale parameters to both datasets 1950–2020  
393 and 1950–2021. Both nonstationary parameters use 5-year smoothed annual-mean GMST as a  
394 covariate, provided by NASA’s GISTEMP<sup>66</sup>. For both datasets, the addition of nonstationarity in  
395 the scale parameter improves the model fit over a stationary-scale fit, based on a Likelihood  
396 Ratio Test (significant at the  $p<0.025$  level for the 1950–2021 dataset, and with  $p=0.267$  for  
397 1950–2020; Table S1), and on comparing Kolmogorov-Smirnov test statistics (Fig. S13, 15). A  
398 comparison of the GEV fits against empirical temperature return periods in 1950–1985 vs. 1986–  
399 2021 visually supports a potential widening (Fig. 4b, Fig. S13). Moreover, as such  
400 nonstationarity would reflect a variability change rather than a mean shift, it may be physically  
401 justified by observed increases in regional temperature skewness since 1979, particularly in June  
402 (Fig. S8, 13). The shape parameter, however, is kept stationary: it corresponds to the shape of the  
403 GEV’s upper tail, and a negative value (as found) indicates a fixed upper bound determining the  
404 highest temperature anomaly possible at a given global temperature, which is likely to be true  
405 based on energetic constraints.

406 For model data, we calculate the maximum June mean among all 14 ensemble members  
407 for each year. We fit a GEV to these ensemble-maximum June means over 1870–2010, with  
408 nonstationary location parameter using 5-year smoothed annual PNWMST as a covariate.  
409 Nonstationarity in GMST does not significantly improve the fits over total stationarity, while  
410 nonstationarity in PNWMST does ( $p<0.1$  and  $p<0.001$  for Prescribed and Interactive SM

411 ensembles, respectively). Fits are presented in Fig. 3 evaluated at 2020's annual PNWMST  
412 (calculated from ERA5) to provide present-day estimates of the 2021 event return periods  
413 without including its information in the PNWMST itself. We repeat the analysis with block size  
414 of 28 and 36 member-years (maxima over 2 and 3 years of data, respectively) and find fairly  
415 consistent results but with drastically increased uncertainty as the total block number decreases.

416 For all GEV results, 95% confidence intervals surrounding return period curves are  
417 shown based on a bootstrapping method, as a non-parametric alternative to a parametric method  
418 using asymptotic standard errors. Bootstrapping is done with a block size of one year, and is  
419 obtained by resampling (drawing  $n$  out of a given  $n$  datapoints with replacement, for 5,000  
420 iterations for model data and 1,000 iterations for observational data) and calculating the desired  
421 output (i.e., return periods as a function of return level) for each iteration. The displayed 95%  
422 confidence interval bounds are taken as the 2.5th and 97.5th percentiles of the resulting return  
423 period curves. (Bootstrapping in Fig. 2 is also done with a one-year block size and 5,000  
424 iterations.)

425

#### 426 **Acknowledgements**

427 We are thankful to Yutian Wu, Radley Horton, Deepti Singh, Colin Raymond, Cassandra  
428 Rogers, and Richard Seager for valuable feedback on this work. We thank Donna Lee for  
429 configuring, running, and making output available from CAM5–GOGA. Support for this work  
430 was provided by NSF-AGS-1934358.

431

#### 432 **Data Availability**

433 All ERA5 output used in this study is available from ECMWF at  
434 <https://cds.climate.copernicus.eu/cdsapp#!/dataset/reanalysis-era5-single-levels>. All  
435 CAM5\_GOGA output used in this study is available at <https://doi.org/10.5281/zenodo.5800726>.  
436 CMIP6 multimodel mean warming levels are available at  
437 <https://doi.org/10.5281/zenodo.4600695>.

438

#### 439 **Code Availability**

440 All figures were produced using Python v.3.6  
441 (<https://www.python.org/downloads/release/python-360/>). All code needed to reproduce the  
442 main figures is available at [https://github.com/sambartusek/pnw\\_hw\\_2021](https://github.com/sambartusek/pnw_hw_2021).  
443

444 **References**

- 445 1. Popovich, N. & Choi-Schagrin, W. Hidden Toll of the Northwest Heat Wave: Hundreds of  
446 Extra Deaths. *The New York Times* (2021).
- 447 2. Excess Deaths Associated with COVID-19.  
448 [https://www.cdc.gov/nchs/nvss/vsrr/covid19/excess\\_deaths.htm](https://www.cdc.gov/nchs/nvss/vsrr/covid19/excess_deaths.htm) (2021).
- 449 3. Coroners. [No title]. [https://www2.gov.bc.ca/gov/content/life-events/death/coroners-](https://www2.gov.bc.ca/gov/content/life-events/death/coroners-service/news-and-updates/heat-related)  
450 [service/news-and-updates/heat-related](https://www2.gov.bc.ca/gov/content/life-events/death/coroners-service/news-and-updates/heat-related).
- 451 4. Schramm, P. J. *et al.* Heat-Related Emergency Department Visits During the Northwestern  
452 Heat Wave - United States, June 2021. *MMWR Morb. Mortal. Wkly. Rep.* **70**, 1020–1021  
453 (2021).
- 454 5. US Census Bureau. American Housing Survey (AHS). [https://www.census.gov/programs-](https://www.census.gov/programs-surveys/ahs.html)  
455 [surveys/ahs.html](https://www.census.gov/programs-surveys/ahs.html).
- 456 6. Tigchelaar, M., Battisti, D. S. & Spector, J. T. Work Adaptations Insufficient to Address  
457 Growing Heat Risk for U.S. Agricultural Workers. *Environ. Res. Lett.* **15**, (2020).
- 458 7. US Drought Monitor Map Archive. <https://droughtmonitor.unl.edu/Maps/MapArchive.aspx>.
- 459 8. National Fire News. <https://www.nifc.gov/fire-information/nfn>.
- 460 9. Silverman, H., Guy, M. & Sutton, J. Western wildfire smoke is contributing to New York  
461 City’s worst air quality in 15 years. *CNN* (2021).
- 462 10. Meehl, G. A. & Tebaldi, C. More intense, more frequent, and longer lasting heat waves in  
463 the 21st century. *Science* **305**, 994–997 (2004).
- 464 11. Perkins-Kirkpatrick, S. E. & Lewis, S. C. Increasing trends in regional heatwaves. *Nat.*  
465 *Commun.* **11**, 3357 (2020).
- 466 12. Philip, S. Y. *et al.* Rapid attribution analysis of the extraordinary heatwave on the Pacific

- 467 Coast. <https://www.worldweatherattribution.org/wp-content/uploads/NW-US-extreme-heat->  
468 2021-scientific-report-WWA.pdf.
- 469 13. Coumou, D. & Robinson, A. Historic and future increase in the global land area affected by  
470 monthly heat extremes. *Environ. Res. Lett.* **8**, 034018 (2013).
- 471 14. Power, S. B. & Delage, F. P. D. Setting and smashing extreme temperature records over the  
472 coming century. *Nat. Clim. Chang.* **9**, 529–534 (2019).
- 473 15. Fischer, E. M., Sippel, S. & Knutti, R. Increasing probability of record-shattering climate  
474 extremes. *Nat. Clim. Chang.* **11**, 689–695 (2021).
- 475 16. Taleb, N. N. *The Black Swan: The Impact of the Highly Improbable*. (Random House  
476 Publishing Group, 2007).
- 477 17. Aven, T. On the meaning of a black swan in a risk context. *Saf. Sci.* **57**, 44–51 (2013).
- 478 18. Lin, N. & Emanuel, K. Grey swan tropical cyclones. *Nat. Clim. Chang.* **6**, 106–111 (2015).
- 479 19. Petoukhov, V., Rahmstorf, S., Petri, S. & Schellnhuber, H. J. Quasiresonant amplification  
480 of planetary waves and recent Northern Hemisphere weather extremes. *Proc. Natl. Acad.*  
481 *Sci. U. S. A.* **110**, 5336–5341 (2013).
- 482 20. Petoukhov, V. *et al.* Role of quasiresonant planetary wave dynamics in recent boreal spring-  
483 to-autumn extreme events. *Proc. Natl. Acad. Sci. U. S. A.* **113**, 6862–6867 (2016).
- 484 21. Screen, J. A. & Simmonds, I. Amplified mid-latitude planetary waves favour particular  
485 regional weather extremes. *Nat. Clim. Chang.* **4**, 704–709 (2014).
- 486 22. Kornhuber, K. *et al.* Summertime Planetary Wave Resonance in the Northern and Southern  
487 Hemispheres. *J. Clim.* **30**, 6133–6150 (2017).
- 488 23. Kornhuber, K. *et al.* Amplified Rossby waves enhance risk of concurrent heatwaves in  
489 major breadbasket regions. *Nat. Clim. Chang.* **10**, 48–53 (2019).

- 490 24. Mann, M. E. *et al.* Influence of Anthropogenic Climate Change on Planetary Wave  
491 Resonance and Extreme Weather Events. *Sci. Rep.* **7**, 45242 (2017).
- 492 25. Mann, M. E. *et al.* Projected changes in persistent extreme summer weather events: The role  
493 of quasi-resonant amplification. *Sci Adv* **4**, eaat3272 (2018).
- 494 26. Kornhuber, K. & Tamarin-Brodsky, T. Future changes in northern hemisphere summer  
495 weather persistence linked to projected arctic warming. *Geophys. Res. Lett.* **48**, (2021).
- 496 27. Hirschi, M. *et al.* Observational evidence for soil-moisture impact on hot extremes in  
497 southeastern Europe. *Nat. Geosci.* **4**, 17–21 (2010).
- 498 28. Miralles, D. G., van den Berg, M. J., Teuling, A. J. & de Jeu, R. A. M. Soil moisture-  
499 temperature coupling: A multiscale observational analysis. *Geophys. Res. Lett.* **39**, (2012).
- 500 29. Miralles, D. G., Teuling, A. J., van Heerwaarden, C. C. & Vilà-Guerau de Arellano, J.  
501 Mega-heatwave temperatures due to combined soil desiccation and atmospheric heat  
502 accumulation. *Nat. Geosci.* **7**, 345–349 (2014).
- 503 30. Rasmijn, L. M. *et al.* Future equivalent of 2010 Russian heatwave intensified by weakening  
504 soil moisture constraints. *Nat. Clim. Chang.* **8**, 381–385 (2018).
- 505 31. Dirmeyer, P. A., Balsamo, G., Blyth, E. M., Morrison, R. & Cooper, H. M. Land-  
506 atmosphere interactions exacerbated the drought and heatwave over northern Europe during  
507 summer 2018. *AGU Advances* **2**, (2021).
- 508 32. Seneviratne, S. I. *et al.* Investigating soil moisture–climate interactions in a changing  
509 climate: A review. *Earth-Sci. Rev.* **99**, 125–161 (2010).
- 510 33. Koster, R. D. *et al.* Regions of strong coupling between soil moisture and precipitation.  
511 *Science* **305**, 1138–1140 (2004).
- 512 34. Cook, B. I., Smerdon, J. E., Seager, R. & Coats, S. Global warming and 21st century

- 513       drying. *Clim. Dyn.* **43**, 2607–2627 (2014).
- 514   35. Cook, B. I., Ault, T. R. & Smerdon, J. E. Unprecedented 21st century drought risk in the  
515       American Southwest and Central Plains. *Sci Adv* **1**, e1400082 (2015).
- 516   36. Dirmeyer, P. A. *et al.* Projections of the shifting envelope of Water cycle variability. *Clim.*  
517       *Change* **136**, 587–600 (2016).
- 518   37. Seneviratne, S. I., Lüthi, D., Litschi, M. & Schär, C. Land-atmosphere coupling and climate  
519       change in Europe. *Nature* **443**, 205–209 (2006).
- 520   38. Petoukhov, V. *et al.* Alberta wildfire 2016: Apt contribution from anomalous planetary  
521       wave dynamics. *Sci. Rep.* **8**, 12375 (2018).
- 522   39. Teng, H. & Branstator, G. Amplification of Waveguide Teleconnections in the Boreal  
523       Summer. *Current Climate Change Reports* **5**, 421–432 (2019).
- 524   40. Schumacher, D. L. *et al.* Amplification of mega-heatwaves through heat torrents fuelled by  
525       upwind drought. *Nat. Geosci.* **12**, 712–717 (2019).
- 526   41. Wang, J. *et al.* Changing lengths of the Four Seasons by global warming. *Geophys. Res.*  
527       *Lett.* **48**, (2021).
- 528   42. Berg, A. *et al.* Impact of Soil Moisture–Atmosphere Interactions on Surface Temperature  
529       Distribution. *J. Clim.* **27**, 7976–7993 (2014).
- 530   43. Swain, D. L., Singh, D., Touma, D. & Diffenbaugh, N. S. Attributing Extreme Events to  
531       Climate Change: A New Frontier in a Warming World. *One Earth* **2**, 522–527 (2020).
- 532   44. van Oldenborgh, G. J. *et al.* Pathways and pitfalls in extreme event attribution. *Clim.*  
533       *Change* **166**, 13 (2021).
- 534   45. Philip, S. *et al.* A protocol for probabilistic extreme event attribution analyses. *Advances in*  
535       *Statistical Climatology, Meteorology and Oceanography* vol. 6 177–203 (2020).



- 536 46. McKinnon, K. A., Rhines, A., Tingley, M. P. & Huybers, P. The changing shape of  
537 Northern Hemisphere summer temperature distributions. *J. Geophys. Res.* **121**, 8849–8868  
538 (2016).
- 539 47. Volodin, E. M. & Yurova, A. Y. Summer temperature standard deviation, skewness and  
540 strong positive temperature anomalies in the present day climate and under global warming  
541 conditions. *Clim. Dyn.* **40**, 1387–1398 (2013).
- 542 48. Philip, S. Y. *et al.* Rapid attribution analysis of the extraordinary heatwave on the Pacific  
543 Coast of the US and Canada June 2021. *Earth Syst. Dyn.* 1–34 (2021) doi:10.5194/esd-  
544 2021-90.
- 545 49. White, R. H., Kornhuber, K., Martius, O. & Wirth, V. From Atmospheric Waves to  
546 Heatwaves: A Waveguide Perspective for Understanding and Predicting Concurrent,  
547 Persistent and Extreme Extratropical Weather. *Bull. Am. Meteorol. Soc.* **-1**, 1–35 (2021).
- 548 50. Xu, P. *et al.* Amplified waveguide teleconnections along the polar front jet favor summer  
549 temperature extremes over northern Eurasia. *Geophys. Res. Lett.* **48**, (2021).
- 550 51. Liu, Y., Sun, C. & Li, J. The Boreal Summer Zonal Wavenumber-3 Trend Pattern and Its  
551 Connection with Surface Enhanced Warming. *Journal of Climate* vol. 35 833–850 (2022).
- 552 52. Dirmeyer, P. A. The terrestrial segment of soil moisture-climate coupling. *Geophys. Res.*  
553 *Lett.* **38**, (2011).
- 554 53. Schwingshackl, C., Hirschi, M. & Seneviratne, S. I. Quantifying Spatiotemporal Variations  
555 of Soil Moisture Control on Surface Energy Balance and Near-Surface Air Temperature. *J.*  
556 *Clim.* **30**, 7105–7124 (2017).
- 557 54. Mueller, B. & Seneviratne, S. I. Hot days induced by precipitation deficits at the global  
558 scale. *Proc. Natl. Acad. Sci. U. S. A.* **109**, 12398–12403 (2012).

- 559 55. Hersbach, H. *et al.* The ERA5 global reanalysis. *Quart. J. Roy. Meteor. Soc.* **146**, 1999–  
560 2049 (2020).
- 561 56. Lee, D. E., Ting, M., Vignaud, N., Kushnir, Y. & Barnston, A. G. Atlantic Multidecadal  
562 Variability as a Modulator of Precipitation Variability in the Southwest United States. *J.*  
563 *Clim.* **31**, 5525–5542 (2018).
- 564 57. Pomposi, C., Giannini, A., Kushnir, Y. & Lee, D. E. Understanding Pacific Ocean influence  
565 on interannual precipitation variability in the Sahel. *Geophys. Res. Lett.* **43**, 9234–9242  
566 (2016).
- 567 58. Neale, R. B. *et al.* The Mean Climate of the Community Atmosphere Model (CAM4) in  
568 Forced SST and Fully Coupled Experiments. *J. Clim.* **26**, 5150–5168 (2013).
- 569 59. Titchner, H. A. & Rayner, N. A. The Met Office Hadley Centre sea ice and sea surface  
570 temperature data set, version 2: 1. Sea ice concentrations. *J. Geophys. Res.* **119**, 2864–2889  
571 (2014).
- 572 60. Hauser, M., Orth, R. & Seneviratne, S. I. Investigating soil moisture-climate interactions  
573 with prescribed soil moisture experiments: an assessment with the Community Earth  
574 System Model (version 1.2). *Geosci. Model Dev. Discuss.* 1–18 (2016).
- 575 61. Humphrey, V. *et al.* Soil moisture–atmosphere feedback dominates land carbon uptake  
576 variability. *Nature* **592**, 65–69 (2021).
- 577 62. Hauser, M. *mathause/cmip\_temperatures: version 0.2.1.* (2021).  
578 doi:10.5281/zenodo.5532894.
- 579 63. Coles, S. *An Introduction to Statistical Modeling of Extreme Values.* (Springer, London,  
580 2001).
- 581 64. Paciorek, C. *climextRemes: Tools for Analyzing Climate Extremes.* (2019).

582 doi:10.5281/zenodo.3240582.

583 65. Bell, B. *et al.* The ERA5 global reanalysis: Preliminary extension to 1950. *Quart. J. Roy.*

584 *Meteor. Soc.* **147**, 4186–4227 (2021).

585 66. Data.GISS: GISS surface temperature analysis (GISTEMP v4).

586 <https://data.giss.nasa.gov/gistemp/>.

587 67. Archambault, H. M., Bosart, L. F., Keyser, D. & Cordeira, J. M. A Climatological Analysis

588 of the Extratropical Flow Response to Recurring Western North Pacific Tropical Cyclones.

589 *Mon. Weather Rev.* **141**, 2325–2346 (2013).

590 68. Stuijvenolt Allen, J., Simon Wang, S.-Y., LaPlante, M. D. & Yoon, J.-H. Three western

591 pacific typhoons strengthened fire weather in the recent northwest U.s. conflagration.

592 *Geophys. Res. Lett.* **48**, (2021).

593 69. Oey, L.-Y. & Chou, S. Evidence of rising and poleward shift of storm surge in western

594 North Pacific in recent decades. *J. Geophys. Res. C: Oceans* **121**, 5181–5192 (2016).

595 70. Sharmila, S. & Walsh, K. J. E. Recent poleward shift of tropical cyclone formation linked to

596 Hadley cell expansion. *Nat. Clim. Chang.* **8**, 730–736 (2018).

597 71. Wang, R. & Wu, L. Influence of Track Changes on the Poleward Shift of LMI Location of

598 Western North Pacific Tropical Cyclones. *J. Clim.* **32**, 8437–8445 (2019).

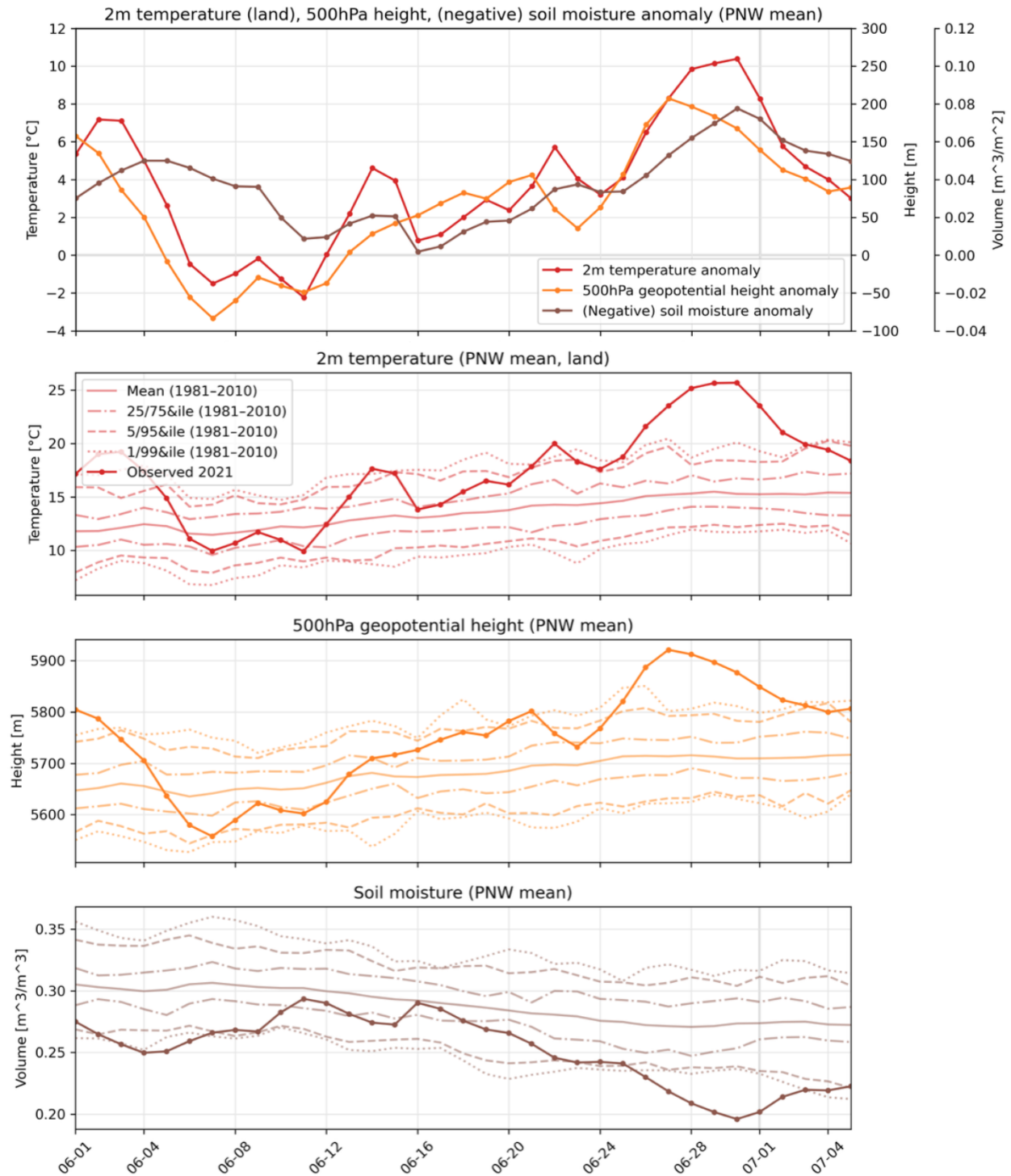
599

600

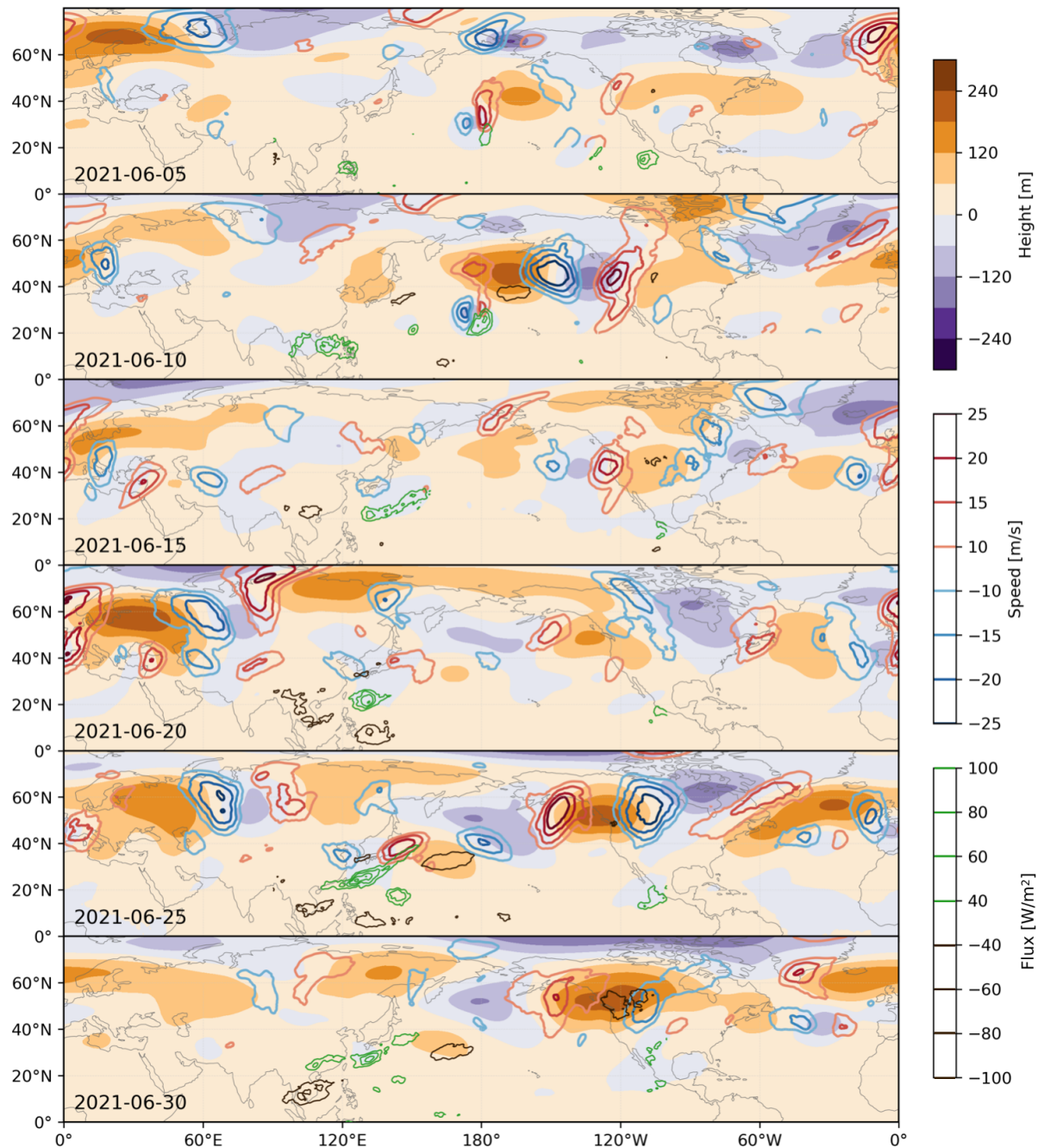
601

602 **Supplementary Information**

603



604 **Fig. S1: PNW anomalies and actual values compared with historical distributions. Top:** As  
 605 in Figure 1d, but anomalies are not standardized. **Bottom three:** PNW-mean actual variable  
 606 values during June 2021 compared with their historical distributions (over 1981–2010).



607 **Fig. S2: Atmospheric dynamics during June 2021 leading to the anomalous geopotential**  
 608 **heights associated with the PNW heatwave. a-f): 500hPa Geopotential height (filled contours),**  
 609 **300hPa meridional wind speed (red and blue contours), and outgoing longwave radiation (OLR;**  
 610 **green and dark brown contours) anomalies averaged over 9-day periods centered on the**  
 611 **annotated date. For clarity, the meridional wind field is only shown poleward of 20°N and the**  
 612 **OLR field is only shown within 90°E–100°W (roughly the Pacific Ocean). a) shows the 9-day**

613 mean surrounding 06/05, when geopotential heights were high in the PNW accompanying a  
614 heatwave, with centers of low and high geopotential height extending westward over the Pacific  
615 and forming a tripole. By 06/10 (**b**) the tripole had expanded longitudinally, placing negative  
616 geopotential height over the PNW, and begun to constitute part of a wavenumber-4 pattern in  
617 meridional wind and geopotential height encircling the midlatitudes. Over 06/10–06/20 (**c–e**)  
618 this wavenumber-4 pattern moved slightly northward and shifted phase longitudinally,  
619 eventually placing high geopotential height over the PNW. Throughout the last two weeks of  
620 June (**d–f**) the wavenumber-4 pattern persisted and amplified, causing extreme temperatures and  
621 dry soils in central Europe, Siberia, and the PNW, and was reinforced by a Rossby wavetrain  
622 emanating from the subtropical western Pacific.

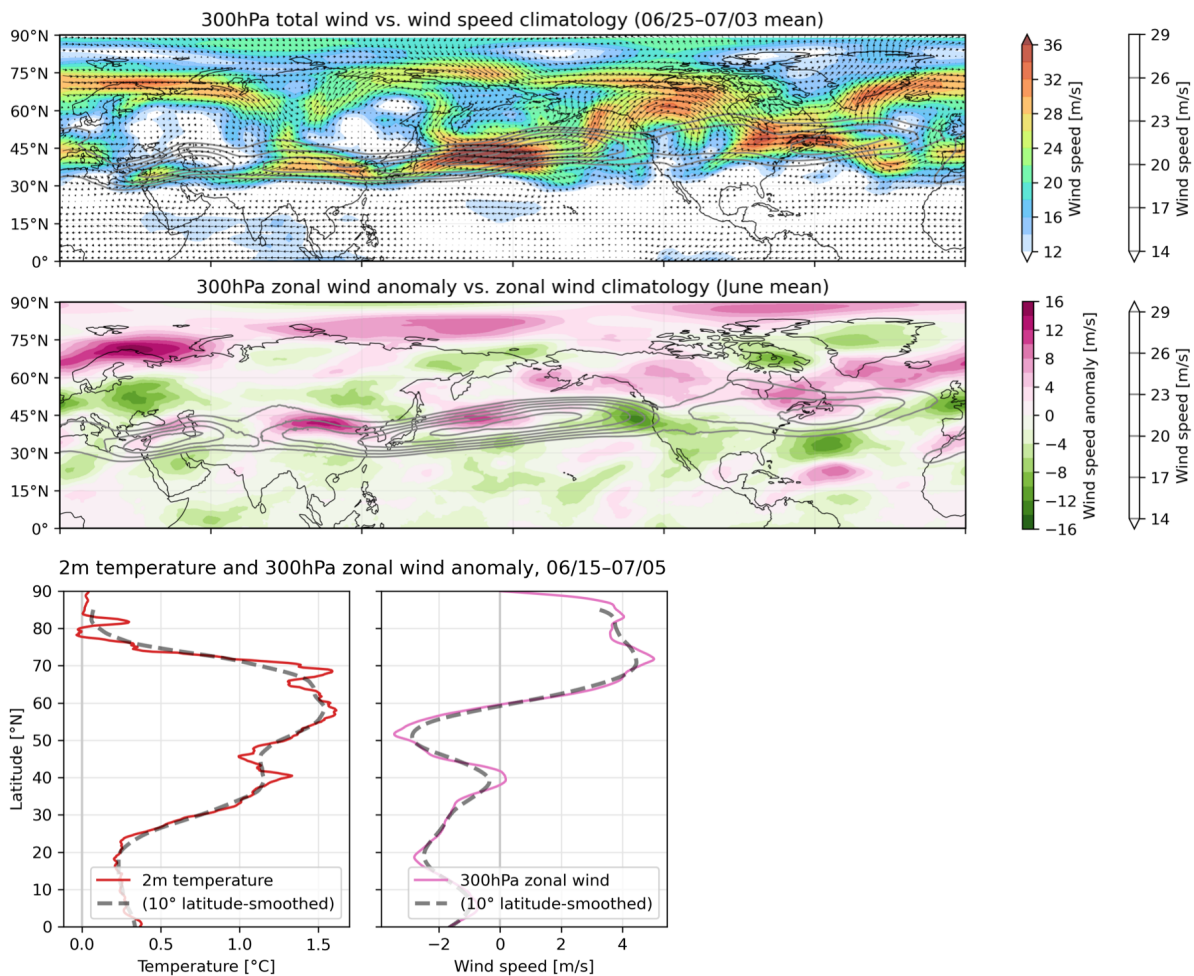
623

624 **Anomalous geopotential heights fueled by the interaction of two distinct Rossby waves**

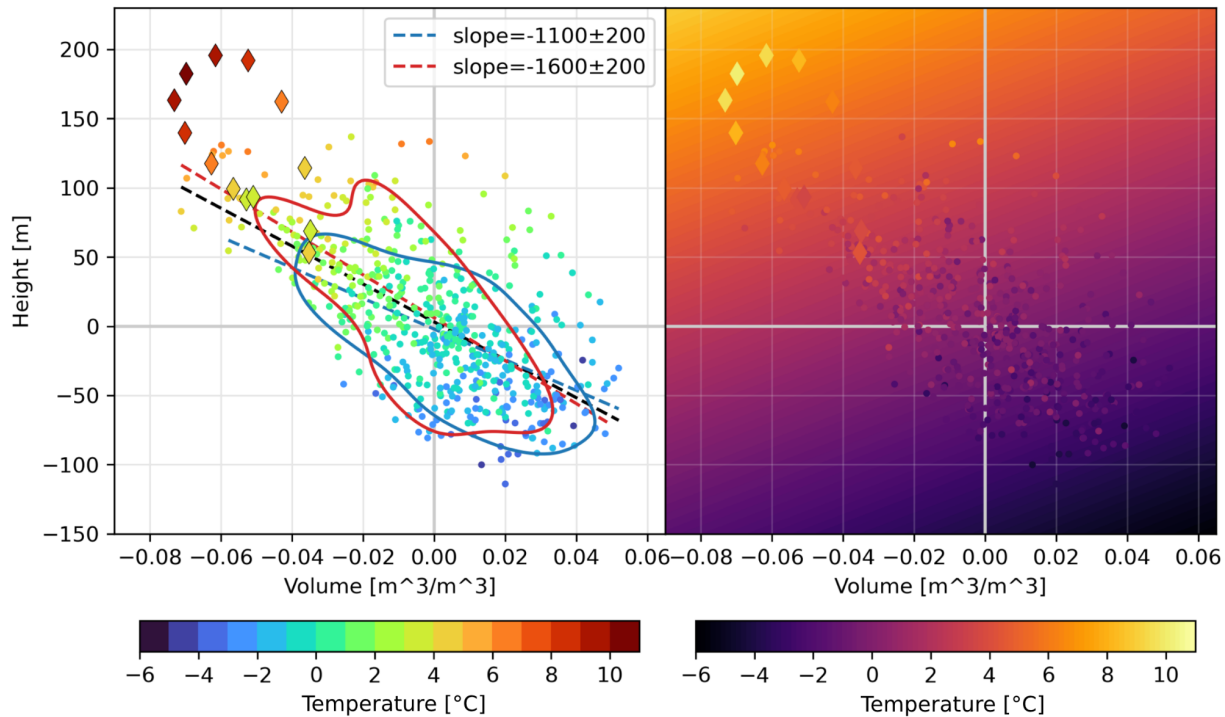
625 Mutually-reinforcing slow- and fast-moving circulation features provided atmospheric dynamical  
626 forcing for the heatwave, each carrying potential climate linkages that may result in increased  
627 risk of concurrency and associated extreme impacts. First, the planetary wavenumber-4  
628 circulation anomaly persisted during much of June, producing synchronized climate extremes  
629 throughout the hemisphere, and dramatically amplified in late June boosting temperatures and  
630 drying soils in the PNW. Accordingly, in late June the jet assumed a persistent anomalous  
631 “wavy” configuration with strong meridional wind meanders (Fig. 2, Fig. S3). Its northern  
632 excursions, encircling anticyclonic anomalies, formed an anomalous polar jet that together with  
633 the subtropical jet created a midlatitude waveguide, and zonal-mean temperature anomalies then  
634 peaked where zonal wind gradients were strongest (~60°N; Fig. S3). These conditions represent  
635 a fingerprint for planetary wave amplification that some evidence suggests may become more  
636 frequent with warming, and may be connected to a weakening meridional temperature  
637 gradient<sup>24,25,39</sup>. Secondly, convection in the western subtropical Pacific (south of Japan)  
638 generated negative outgoing longwave radiation (OLR) anomalies, exciting a late-June Rossby  
639 wavetrain extending towards North America. This synoptic wavetrain locked phase with the  
640 existing hemispheric wave, amplifying the PNW’s geopotential height and temperature  
641 anomalies and perhaps also strengthening the hemispheric wave (Fig. S2). Recent findings show  
642 that typhoons undergoing extratropical transition south of Japan can heighten PNW wildfire risk  
643 by inducing downslope easterly winds across the Cascade Range that adiabatically warm and

644 dry<sup>67,68</sup>, as demonstrated during 2021<sup>48</sup>. A projected northward shift in typhoon tracks in this  
645 region under global warming<sup>69-71</sup> could increase the risk of such events.





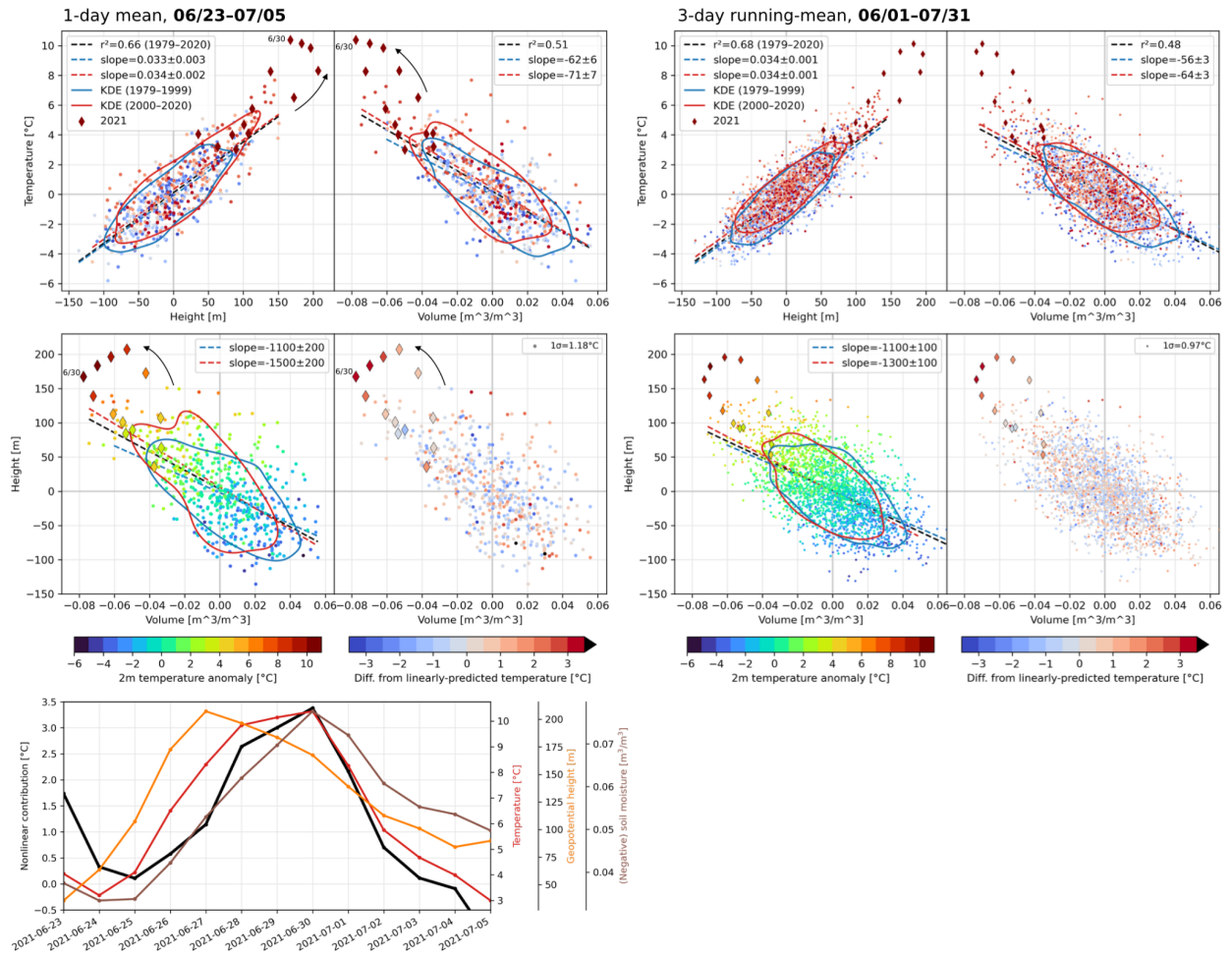
646 **Fig. S3: Total wind, zonal wind, and temperature anomalies in summer 2021. Top:**  
647 **anomalous total wind over 06/25–07/03, with direction in vectors and magnitude in vectors and**  
648 **color, compared with climatological total wind speed in gray contours. Middle: June-mean**  
649 **anomalous zonal wind in color compared with climatological zonal wind in gray contours.**  
650 **Bottom: 06/15–07/15-mean 2m temperature and zonal wind anomalies and their 10-degree**  
651 **smoothings.**  
652



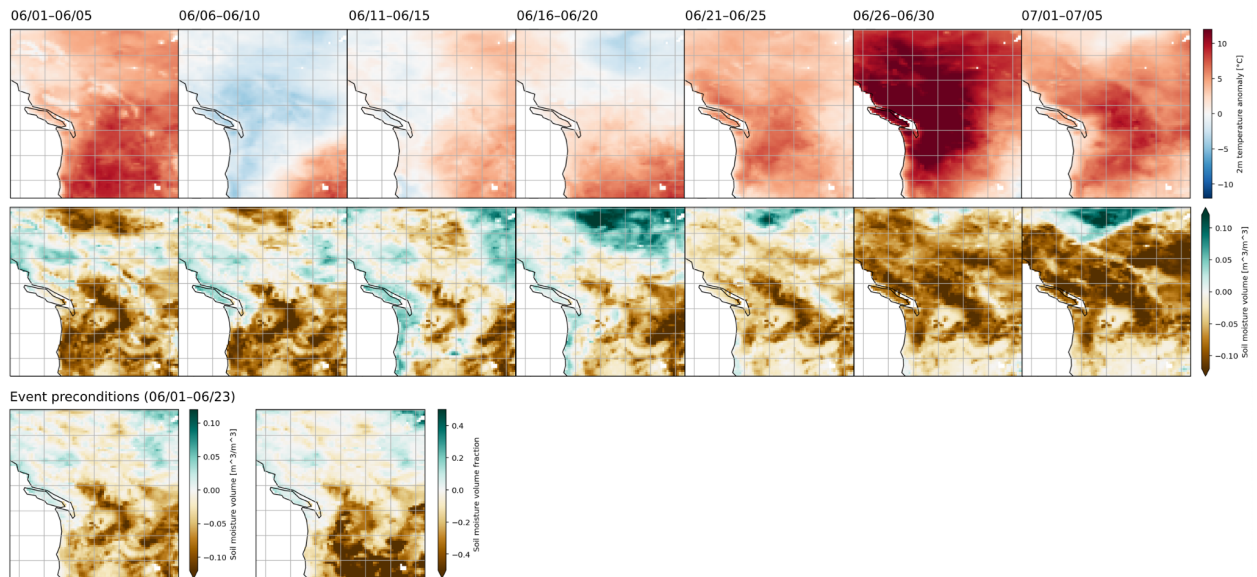
653

654 **Fig. S4: Comparison of observed temperature versus multiple linear regression prediction.**

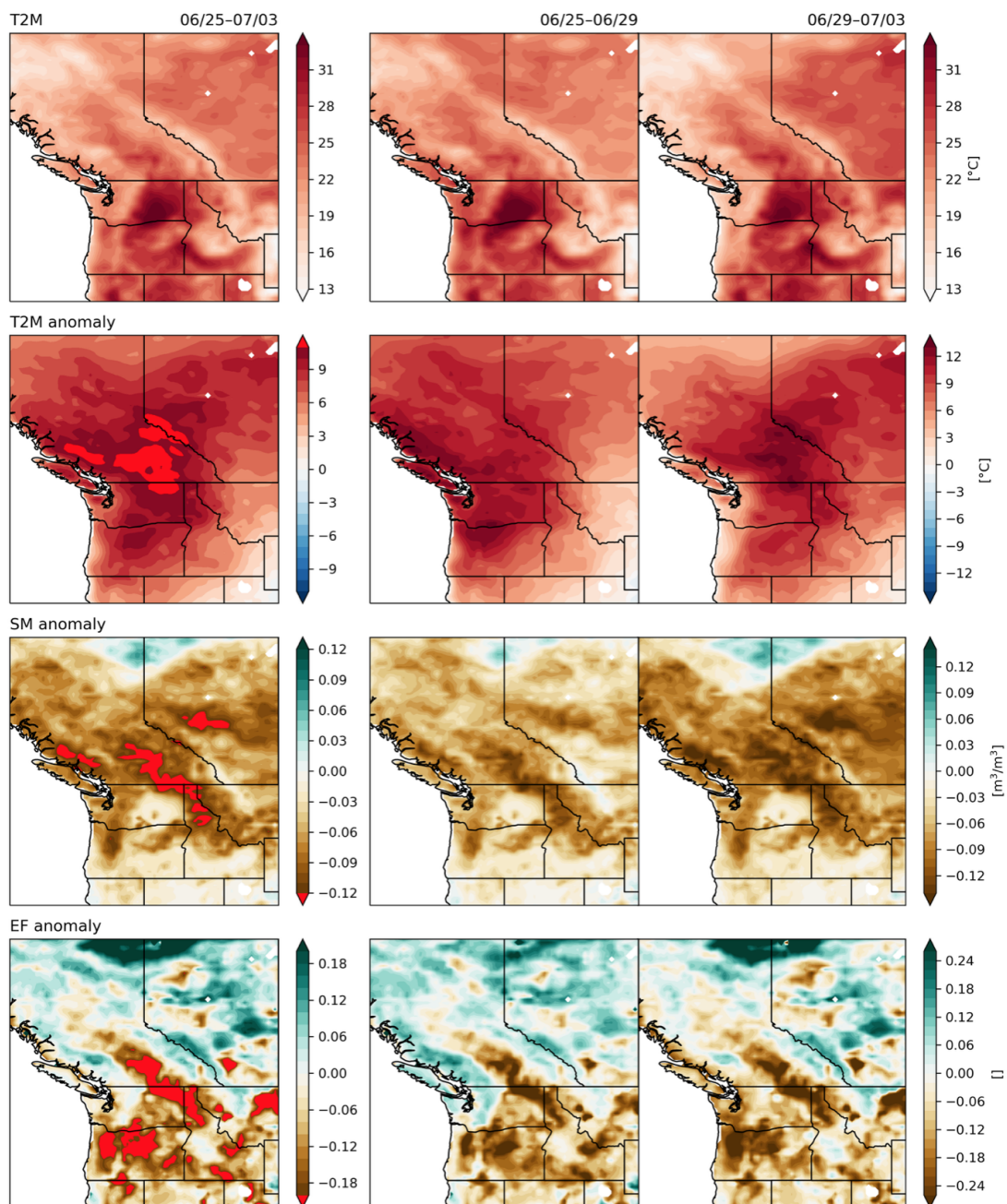
655 **Left panel:** copied from Figure 3 for ease of interpretation. **Right panel:** in the background  
 656 gradient, the temperature modeled by a multiple linear regression based on both soil moisture  
 657 and geopotential height anomalies, with the regressions calculated from the 3-day mean data  
 658 over 06/23–07/05 from 1979–2020. The point data show observed temperatures (i.e., the same  
 659 values as shown in the left panel, but according to a different colormap), with dots for 1979–  
 660 2020 and diamonds for 2021. The difference between the observed temperature (scattered point  
 661 data) and the predicted temperature (the background gradient value underlying each scattered  
 662 point) is what is shown in Figure 2d.



663 **Fig. S5: Top:** As in Figure 2a–d but for daily mean data over 06/23–07/05 (left) and 3-day  
 664 running mean data over 06/01–07/31 (right). **Bottom:** daily mean time series of the nonlinear  
 665 contribution term, temperature, geopotential height, and soil moisture anomalies throughout the  
 666 heatwave.



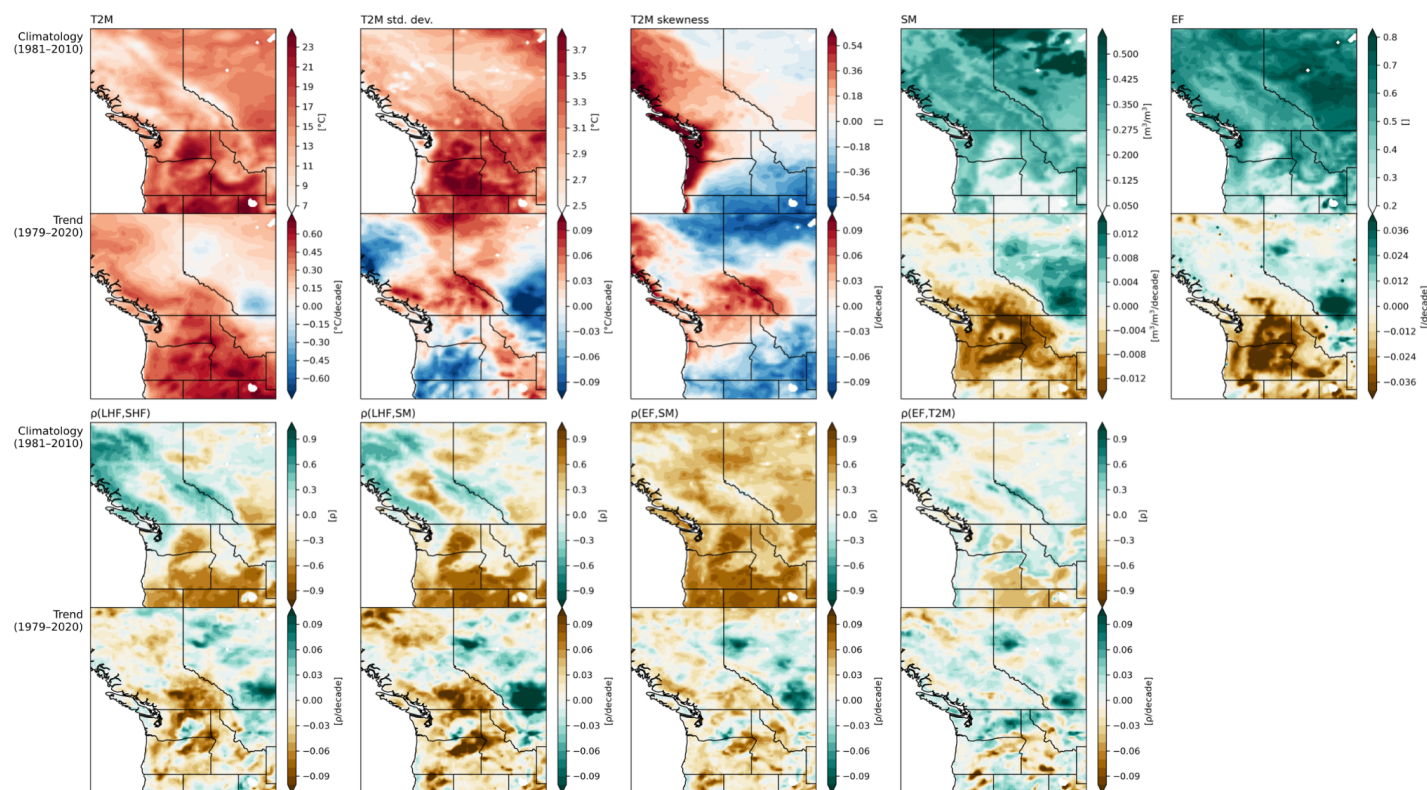
667 **Fig. S6: June evolution of temperature and soil moisture anomalies and soil preconditions**  
 668 **for the late-June heatwave. Top row:** 5-day means of (land) temperature anomalies over the  
 669 PNW from 06/01 to 07/05. **Second row:** as in top row but for soil moisture anomalies. **Bottom**  
 670 **row:** 06/01–06/23 mean soil moisture anomalies over the PNW (left) and the same data  
 671 expressed as fraction of climatology (right), emphasizing large fractional anomalies where soil  
 672 moisture is climatologically low and therefore non-fractional anomalies are limited in magnitude  
 673 compared to wetter areas. (I.e., soil moisture anomalies in Figure 1c show comparatively small  
 674 dry anomalies in the southwest US despite its deep long-term drought, versus the PNW.)



675 **Fig. S7: PNW land-atmosphere anomalies during the 2021 heatwave.** Mean conditions over  
 676 the whole 9-day heatwave period (06/25–07/03; **left column**), its first half (06/25–06/29; **middle**  
 677 **column**), and its second half (06/29–07/03; **right column**), for 2m temperature (T2M) (**top**  
 678 **row**), T2M anomalies (**second row**), soil moisture (SM) anomalies (**third row**), and evaporative  
 679 fraction (EF) anomalies (**bottom row**). EF is calculated from daily-mean latent heat flux (LHF)  
 680 and sensible heat flux (SFH) as  $LHF/(SHF+LHF)$ . Many of the regions of hottest (absolute) T2M  
 681 and hottest T2M, driest SM, and lowest EF anomalies during this heatwave overlapped,

682 particularly in the center of the region: across northern Oregon, eastern Washington, northern  
683 Idaho, and central southern British Columbia (the Interior Plateau). However, some of the largest  
684 T2M anomalies were associated with high EF anomalies instead—mostly in the Coastal and  
685 Cascade mountains on the British Columbia coast and the Cariboo and Monashee mountains  
686 between British Columbia and Alberta. This pattern is very consistent with climatological daily  
687 correlation between EF and T2M anomalies (see Fig. S8): areas where EF and T2M are anti-  
688 correlated (both typically and during this event) tend to be warmer, non-mountain areas with  
689 relatively low soil moisture and Mediterranean and/or semi-arid climates (i.e., across much of  
690 eastern Oregon and Washington (the Columbia Plateau), Idaho, and British Columbia's Interior  
691 Plateau. Therefore, overall, throughout the heatwave, the spatial anti-correlation between EF and  
692 T2M anomalies was very weak, reflecting the diversity of land types and land-atmosphere  
693 coupling regimes across the large region. Overall, the spatial correlation between 9-day-mean  
694 (06/25–07/03) EF and T2M during the heatwave was highly significant but very weak, yielding  
695  $r=-0.04$  with  $p<0.005$ . However, where T2M was both anomalously and climatologically high,  
696 EF and T2M were more tightly anti-correlated. Masking to retain only land regions under the  
697 850hPa level, the spatial correlation was  $-0.24$ , with  $p<0.0001$ .

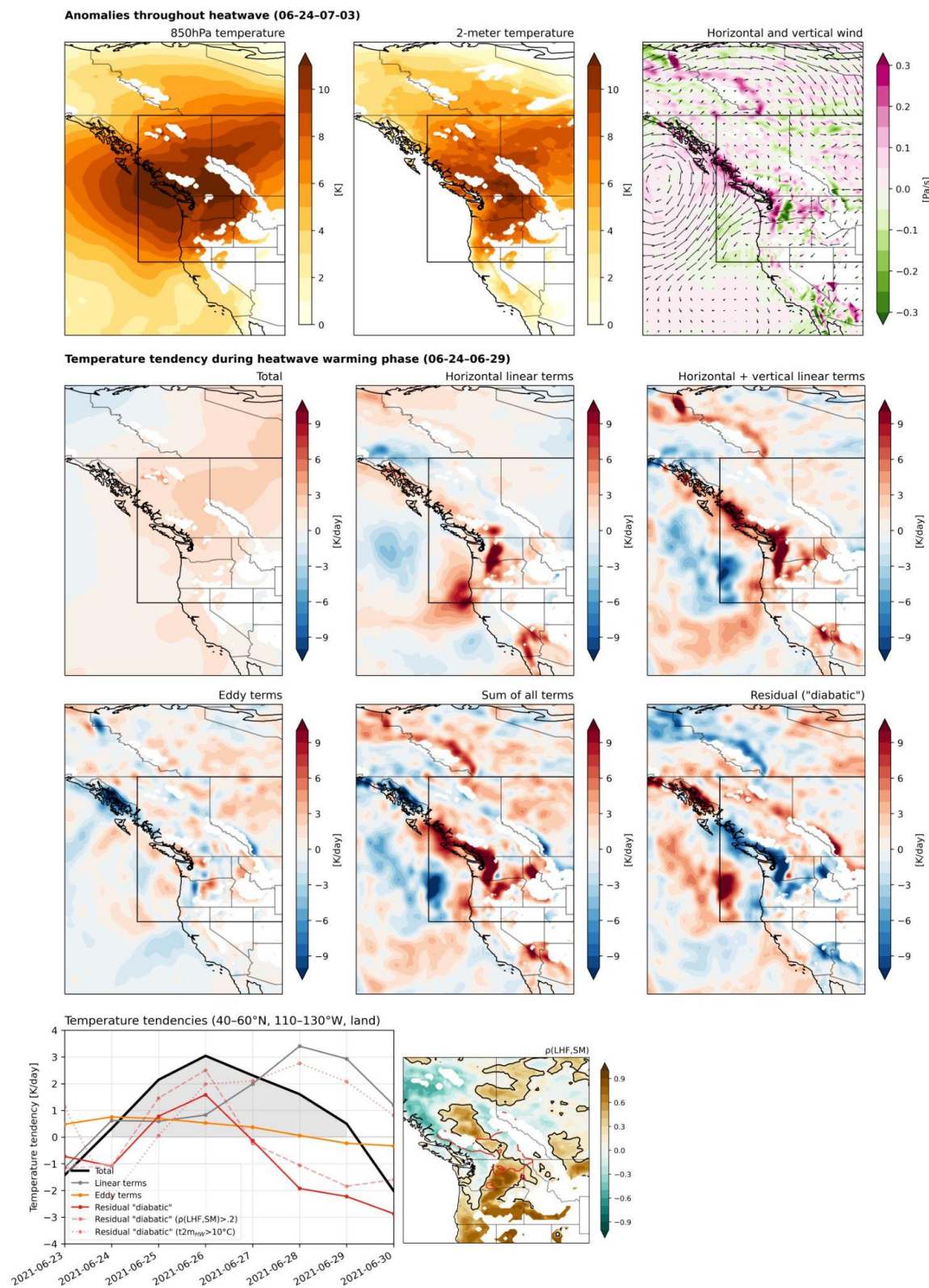
698



699 **Fig. S8: Climatologies and trends of PNW temperature variability, land surface quantities,**  
 700 **and land-atmosphere coupling climatologies and trends. Top row: 1981–2010 June–July**  
 701 **climatologies (top panels) and 1979–2020 linear trends (bottom panels) of 2m temperature**  
 702 **(T2M), T2M variability, soil moisture (SM), and evaporative fraction (EF). T2M standard**  
 703 **deviation and skewness are intra-annual, measuring the within-year variability of daily anomalies**  
 704 **(taken from the 1981–2010 daily climatology). EF is calculated from daily latent heat flux (LHF)**  
 705 **and sensible heat flux (SHF) as  $LHF/(LHF+SHF)$ . Climatologies are calculated using only 1981–**  
 706 **2010 data. Trends consider 1979–2020 and are presented in per-decade units. **Bottom row:****  
 707 **Climatologies and trends of four metrics of land-atmosphere coupling: correlations between LHF**  
 708 **and SHF, LHF and SM, EF and SM, and EF and T2M. At each gridpoint, a correlation**  
 709 **climatology is created by taking daily anomalies (from the daily 1981–2010 climatology) for**  
 710 **each variable during June–July 1979–2020, removing their 1979–2020 linear trends, and**  
 711 **correlating two variables against each other throughout all June–July 1981–2010 days.**  
 712 **Correlation trends are determined by calculating correlations within each year (June–July)**  
 713 **separately, and finding a linear trend in yearly correlation values over 1979–2020 at each**  
 714 **gridpoint. Results are consistent if trends are estimated by subtracting the correlation over 1979–**

1999 from that over 2000–2020. The first three correlations represent the terrestrial component of land-atmosphere coupling while  $\rho(\text{EF}, \text{T2M})$  represents the total feedback pathway. While SM and T2M are nearly everywhere anticorrelated, these correlations show where soil moisture deficit may causally affect T2M. Areas where LHF and SHF are anticorrelated, LHF and SM are correlated, EF and SM are correlated, and EF and T2M are anticorrelated indicate “moisture-limited” regimes with potentially stronger land-atmosphere coupling (as distinct from “energy-limited” regimes where the atmosphere dominantly controls land-surface processes). Such correlation directionalities are typical of “transitional” climate zones between wet and dry: in wet enough areas, soil moisture deficits do not affect evapotranspiration (near-zero  $\rho(\text{EF}, \text{SM})$ ) because a non-limited supply of moisture allows LHF to increase in response to atmospheric heating (positive  $\rho(\text{LHF}, \text{SHF})$  and negative  $\rho(\text{LHF}, \text{SM})$ )—conversely, if SM is lower, LHF is limited and thus EF (LHF’s proportion of total flux) decreases (positive  $\rho(\text{EF}, \text{SM})$  and  $\rho(\text{LHF}, \text{SM})$  and negative  $\rho(\text{LHF}, \text{SHF})$ ). In moisture-limited evapotranspiration areas, decreased EF (i.e., increased SHF partition of total flux) can raise T2M, allowing for positive land-atmosphere feedbacks as raised T2M can further decrease SM, increase SHF, decrease LHF, and decrease EF. Such areas climatologically extend from the drier interior central West, to the Columbia Plateau in eastern Washington, and even into the British Columbia Interior Plateau (bottom row, top panels). Trends over 1979–2020 indicate that much of the PNW is has undergone strengthening in at least the terrestrial component of land-atmosphere coupling— notably, mostly where soil moisture is climatologically moderate as opposed to extremely low (where further drying may instead decrease such correlations), which includes much of BC’s Interior Plateau, much of the Cascade Range region (including Portland and near Seattle) and to the east of the Columbia Plateau. Trends in  $\rho(\text{EF}, \text{T2M})$  indicate that in some of these areas (mostly in the southern PNW but including some of the BC Interior Plateau), T2M itself has become more coupled to EF, potentially signifying increased feedbacks—but overall, such trends have not conclusively emerged. The spatial pattern of trends toward stronger land-atmosphere coupling correspond relatively well with warming, drying SM, and decreasing EF, and in some places with increasing T2M variability: areas of increasing T2M standard deviation and skewness correspond better to land-atmosphere correlation trends than to SM or EF trends alone. (Increasing skewness is furthermore detectable at the regional level; see Fig. S14.)





745 **Fig. S9: Temperature tendency budget analysis at 850hPa. Top row: Temperature (at 850hPa**  
 746 **and 2 meters) and wind (horizontal and vertical) anomalies averaged during the heatwave**

747 (06/24–07/03). The black box shows the region focused on in the manuscript. **Middle rows:**  
748 Spatial patterns of temperature tendency contributions from various (grouped) terms in the  
749 temperature budget, conducted at the 850hPa level and averages during the heatwave warming  
750 phase (06/24–06/29). The residual “diabatic” term is calculated as the total tendency minus the  
751 sum of all non-diabatic terms, and indicates processes not accounted for by the non-diabatic  
752 terms that may in part be attributed to land-atmosphere processes. **Bottom row:** Temporal  
753 evolution of grouped terms in the budget over the course of the heatwave warming period  
754 (06/24–06/29), averaged over the black box in the maps above. Solid lines show the total  
755 heating, the sum of all linear non-diabatic terms, the sum of all eddy non-diabatic terms, and the  
756 residual term. Additionally, we show the residual term averaged over two sub-regions (broken  
757 lines). The dashed line shows the term only where the long-term daily correlation between latent  
758 heat flux (LHF) and soil moisture (SM) exceeds 0.2 (designated by the black contour in the  
759 map). The dotted line shows the term only where the heatwave-averaged (06/25–07/03) 2-meter  
760 temperature anomaly exceeded 10°C (red contour on map). The map background is the same as  
761 that shown in Fig. S8, with altitudes above the 850hPa level masked.

762

### 763 **Temperature Budget Analysis**

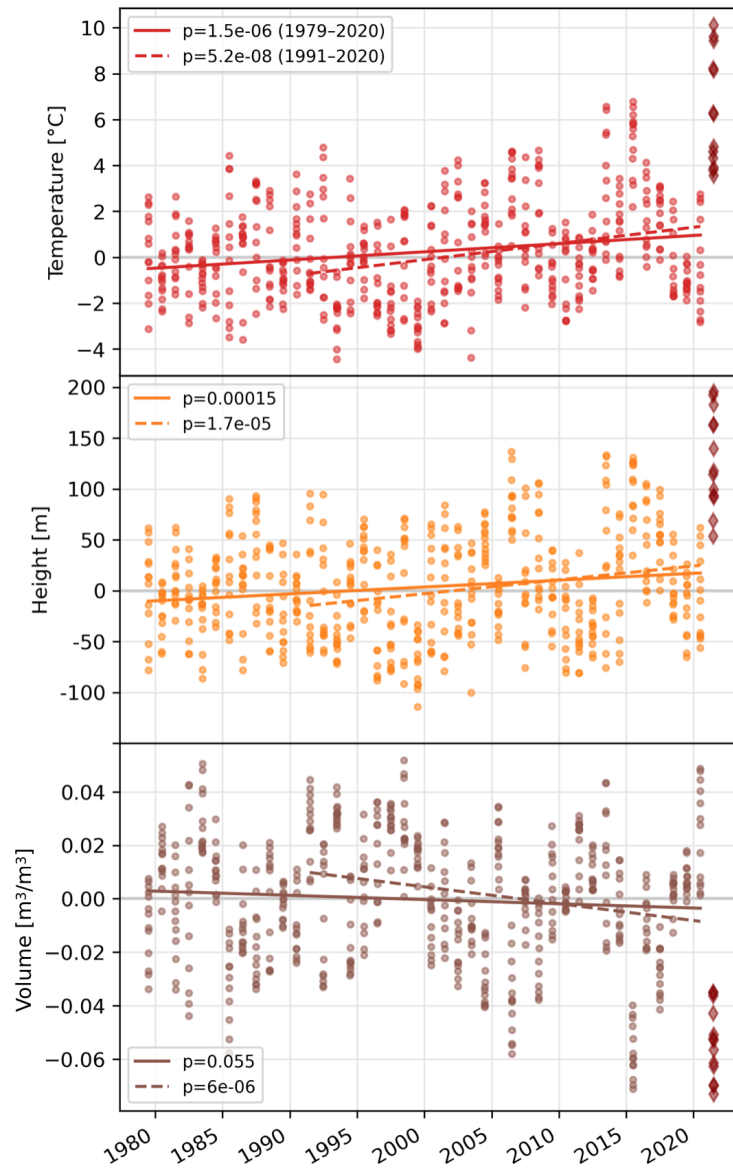
764 We first present a comparison of temperature anomalies averaged throughout the heatwave  
765 (06/24–07/03) at both 2 meters and 850hPa, showing similar geographical patterns with the most  
766 intense anomalies centered over interior British Columbia and eastern Washington. Horizontal  
767 and vertical wind anomalies are also shown, notably displaying easterly anomalies over the  
768 Cascades in western Washington and Oregon, accompanied by upwind ascent and downwind  
769 descent. Given the complex topography in the region, we next perform a temperature budget  
770 analysis at the 850hPa level, using the methodology of He and Black (2016, Heat budget analysis  
771 of Northern Hemisphere high-latitude spring onset events, *J. Geophys. Res. Atmos.*, 121,  
772 10,113–10,137, doi:10.1002/2015JD024681).

773 Overall, at the 850hPa level, we find heterogeneous patterns and strong canceling  
774 between large terms in the temperature budget equation. Throughout the heatwave warming  
775 period (06/24–06/29), horizontal advection clearly contributes to heating along the Cascades but  
776 is opposed in many areas by vertical terms and eddy terms, and remains overall slightly negative  
777 in the interior British Columbia and eastern Washington plateau regions, where temperature

778 anomalies were highest (both at 2 meters and 850hPa). Adiabatic compression and vertical  
779 advection strongly oppose each other in many areas, and when added to the horizontal linear  
780 terms, heating is strong along the Cascades and the immediate coastal mountains of British  
781 Columbia, but still near zero (and even negative in places) in the interior Plateaus of British  
782 Columbia and eastern Washington. Eddy terms are noisy (even at the smoothed spatial scale  
783 presented here, with a 4-grid-cell or  $\sim 1^\circ$  smoother) and contribute both heating and cooling.  
784 Altogether, a time-averaged “diabatic” term (estimated as a residual of all non-diabatic budget  
785 terms from the total temperature tendency) indicates that unaccounted-for diabatic processes may  
786 have been important to the total heating, notably in the interior British Columbia and Columbia  
787 Plateaus, where we have argued that EF and T anomaly correspondence indicates potential  
788 feedback activity and where temperature anomalies were highest. We finally note that because  
789 this budget analysis was undertaken at the 850hPa level, it may potentially underestimate land-  
790 surface processes.

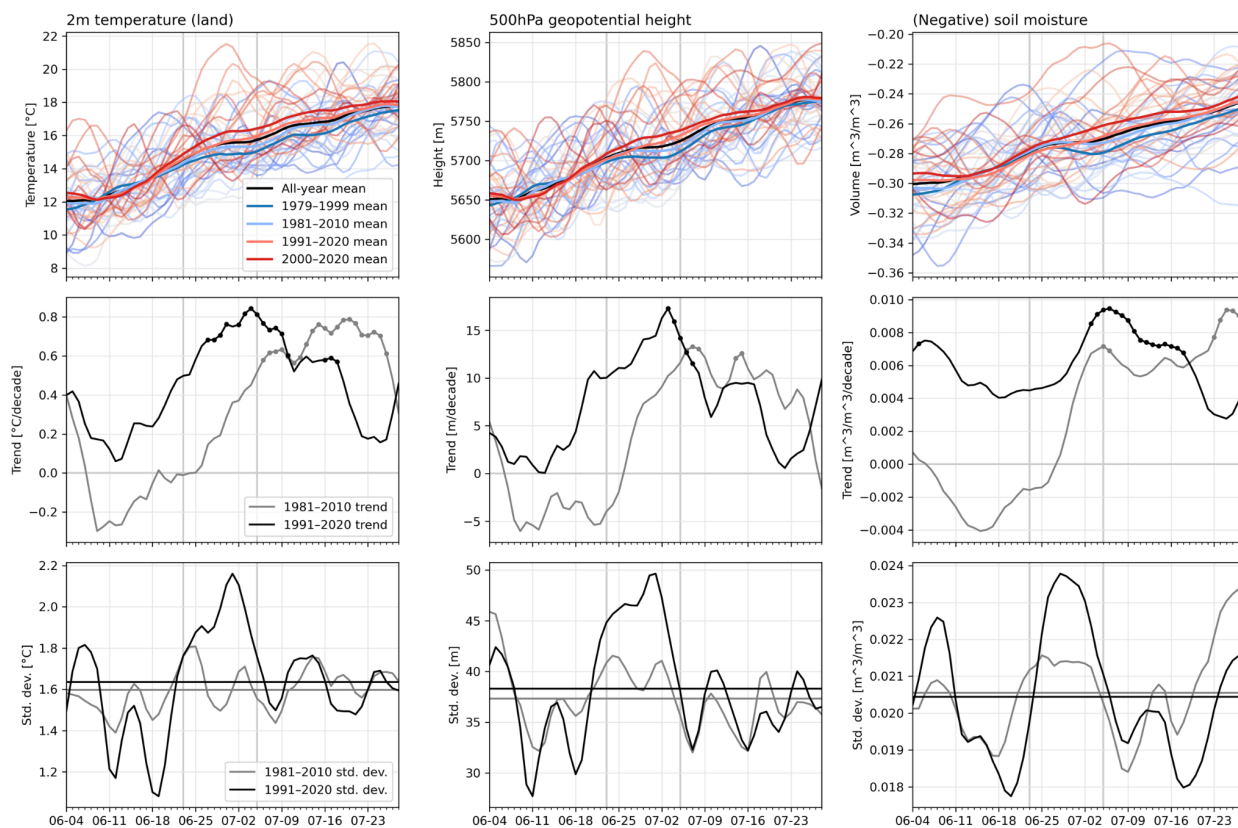
791         A temporal view of some aggregated terms of the heat budget shows that on the days of  
792 maximum heating, the residual term played a large warming role, providing above 50% of the  
793 heating on the maximum day (06/27). It later became negative as the linear terms strengthened,  
794 and heating overall weakened (but as the actual temperature anomalies increased). Subsetting for  
795 areas where historical latent heat flux and soil moisture anti-correlation indicates that land-  
796 atmosphere feedbacks may be typical (black contour on map;  $\rho(\text{LHF}, \text{SM}) > 0.2$ ), the residual  
797 term strengthens, indicating that these areas may be especially responsible for the residual  
798 effects. Furthermore, subsetting by where t2m anomalies throughout the heatwave (06/24–07/03)  
799 reached over  $10^\circ\text{C}$ , the residual term is greatly strengthened specifically in the later days of  
800 heating (06/27–06/29). This helps corroborate that the residual term is especially active in the  
801 regions experiencing the most extreme heat, where feedbacks may have been strongest. Both  
802 subsets help narrow down what specific processes may be responsible for this residual term.

803



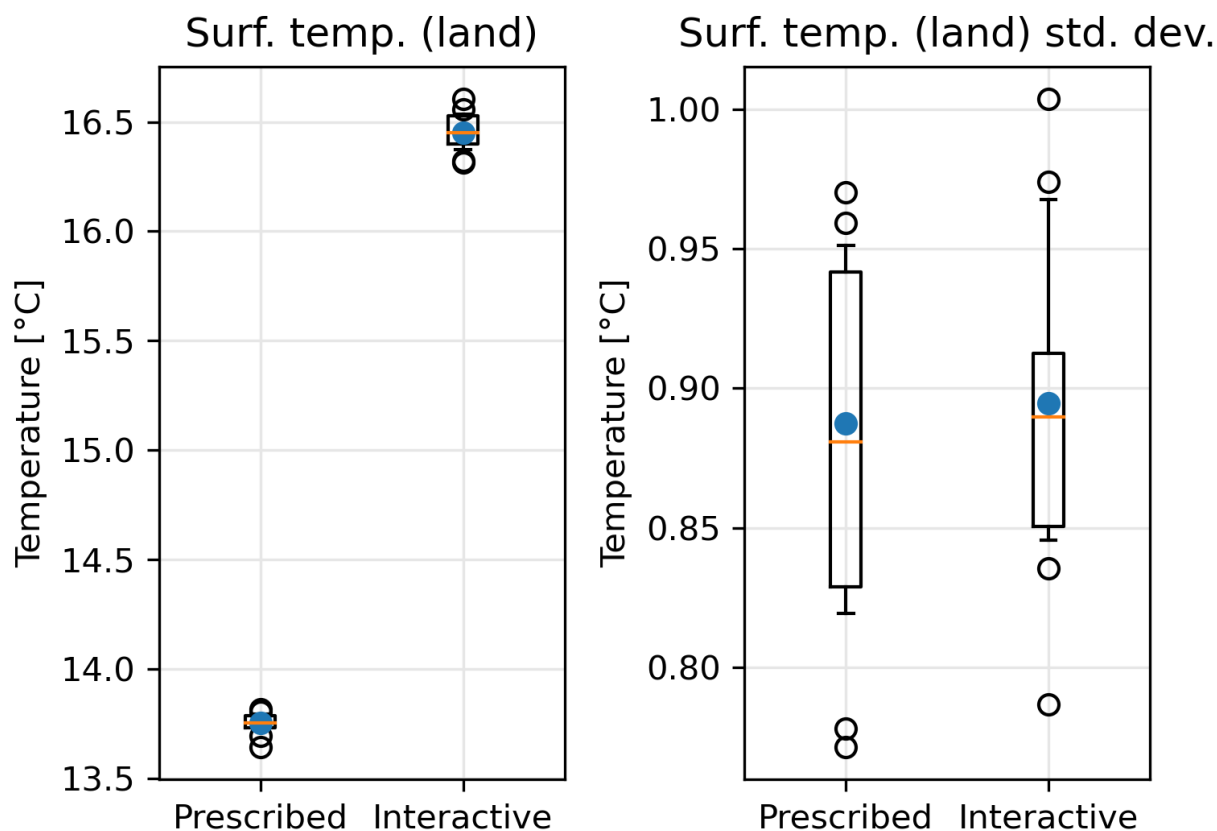
804 **Fig. S10:** The same data as in Fig. 2 plotted against year, shown individually for temperature  
 805 (**top**)), geopotential height (**middle**)), and soil moisture (**bottom**)), and linear trends over 1979–  
 806 2020 and 1991–2020 (with p-values in legends).

807



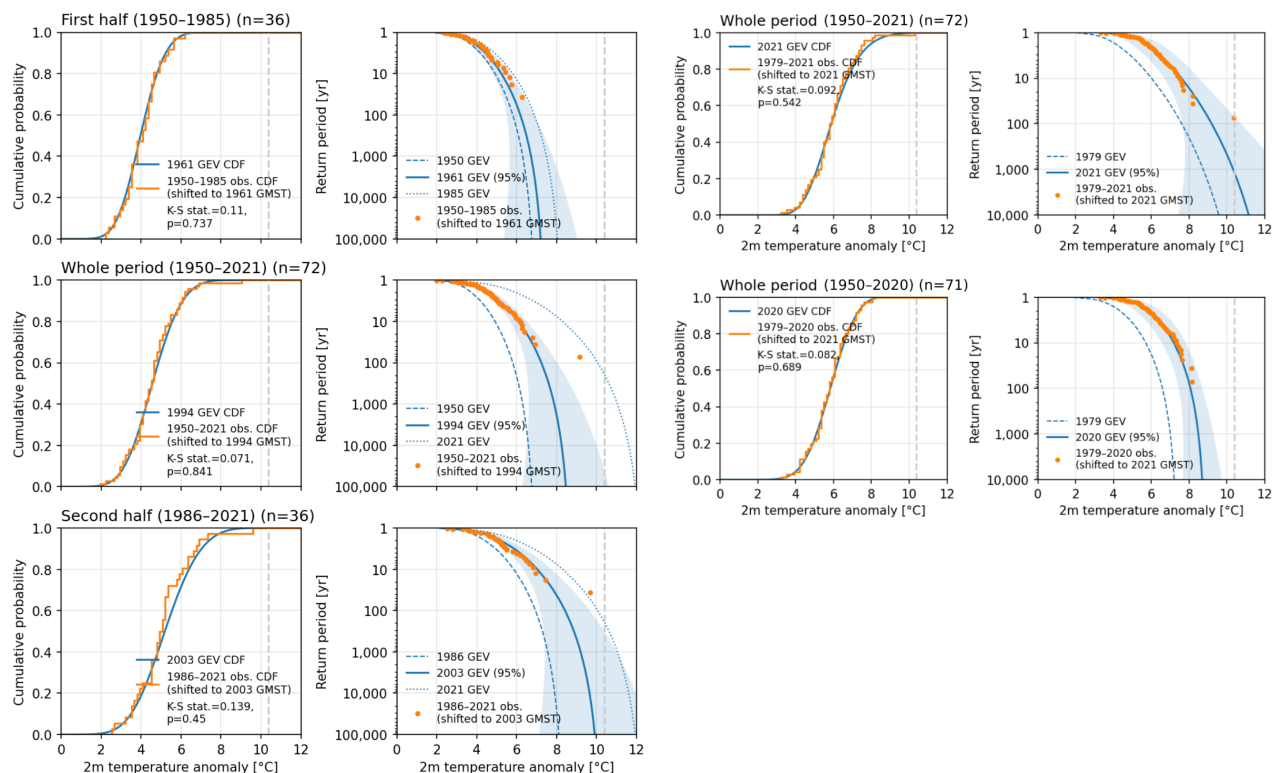
808 **Fig. S11: Historical changes in temperature, geopotential height, and soil moisture and**  
 809 **their interannual variability.** PNW-mean raw (i.e., non-anomalous) temperature, geopotential  
 810 height, and soil moisture data from ERA5 over the entire period of analysis except 2021 (1979–  
 811 2020, throughout June and July). All data are 7-day running means. Gray vertical bars mark  
 812 06/23 and 07/05. **Top row:** color-coded data for each year (blue in 1979 to red in 2020), with  
 813 means throughout the various analysis periods overlaid according to the legend. Second row:  
 814 linear trends in data over 1981–2010 and 1991–2020, marked with dots where significant at 90%  
 815 level. **Bottom row:** interannual standard deviations across 1981–2010 and 1991–2020, with  
 816 horizontal lines demarcating the June–July mean for each period. The bottom row shows that in  
 817 the PNW, standard deviation is increasing for temperature and geopotential height over June and  
 818 July as a whole, and especially for late-June–early-July (when soil moisture standard deviation is  
 819 also increasing sharply)—which is likely associated with warming trends shifting earlier in the  
 820 year in accordance with an advancing summer onset (as illustrated in the left panel of the middle  
 821 row).

### June-mean PNW-mean:



822

823 **Fig. S12: Shift and variability changes of June-mean PNW-mean temperature in the model**  
 824 **experiment.** Boxplots show the model member spread, with the two most distant members  
 825 towards either end of the 14-member distribution shown as individual dots. Blue dots show the  
 826 ensemble total (all member-months) and orange lines show the ensemble mean. The left plot is  
 827 the mean surface temperature, and the right plot is the surface temperature standard deviation.  
 828 All standard deviations are calculated internally for each member, i.e., across each member's  
 829 entire 1870–2010 run.

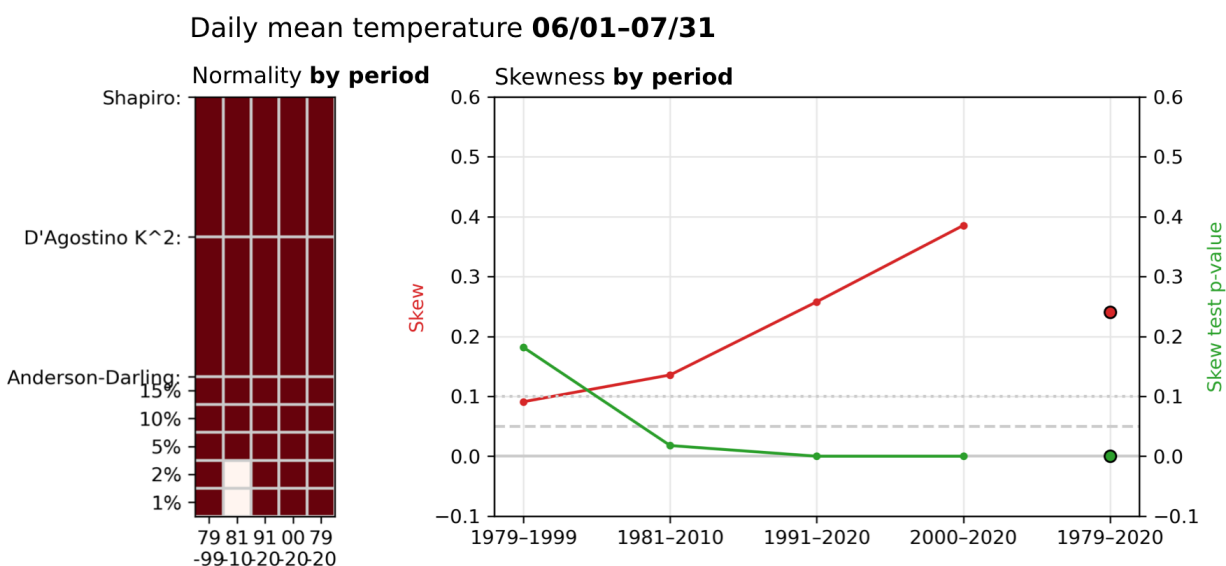


830 **Fig. S13: Validation of nonstationary-scale GEV fits including the 2021 observation (first**  
 831 **two columns), and stationary-scale fits (second two columns). First column:** For each period,  
 832 empirical CDFs of observations in that period (orange) are compared with the nonstationary-  
 833 scale GEV fit CDF (blue) evaluated at the mean GMST of that period. Results of a Kolmogorov-  
 834 Smirnov test (D statistic and p-value), testing whether the samples can be determined as drawn  
 835 from different distributions, are indicated in the legends. No p-values are low enough to reject  
 836 the GEV fits even with the inclusion of 2021. **Second column:** For each period, empirical return  
 837 periods (orange dots) are compared with GEV-derived return periods (blue curves) evaluated at  
 838 the mean GMST of the period. Empirical return periods are estimated as  $1/(1-i/(n+1))$ , with  $n$  the  
 839 number of observations in each period and  $i$  their ranking in ascending temperature order. In both  
 840 columns, the observations' raw temperatures are "shifted", based on the location parameter's  
 841 dependence on GMST, to each period's mean GMST (for example, the highest temperature  
 842 observation in the lower right plot, representing the 2021 heatwave, is shifted down from its raw  
 843 temperature [the dashed gray line], to the median GMST of 1986–2021, seen in 2003; compare  
 844 with Fig. 4b to see that mean and median are indistinguishable). Shifting observations by GMST  
 845 in this way still does not account for any variability changes (i.e., only considers location  
 846 parameter nonstationarity, not scale parameter nonstationarity), so K-S tests may even

847 overestimate the true difference between GEV fits and observations. **Third and fourth**  
848 **columns:** As in first two columns but for the stationary-scale-parameter GEV fit both including  
849 (top) and excluding (bottom) 2021 (both covering the whole time period, as observations can  
850 simply be shifted based on location parameter while their scale is fixed).



851  
852

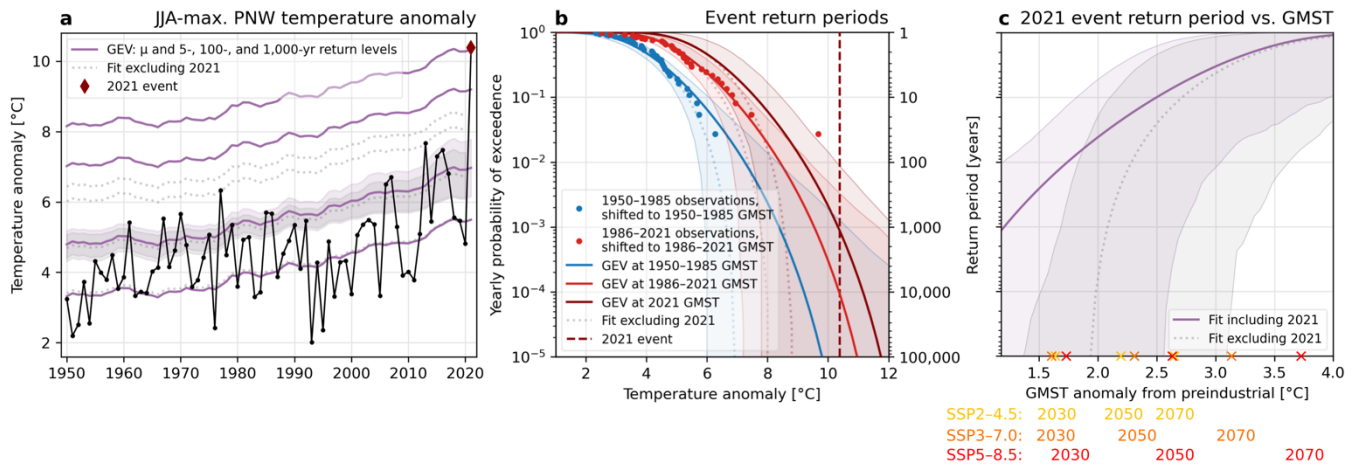


853

854 **Fig. S14: Skew tests for temperature anomaly distributions over historical periods. Top**  
 855 **row:** for daily mean temperature anomalies over 06/23–07/05, the plots show results from three  
 856 normality tests determining whether the dataset (individual days over the 1981–2010 period (left)  
 857 and 1991–2020 period (right)) can be statistically distinguished from normal (red) or not (white).  
 858 Shapiro and D’Agostino tests report a single output, and the Anderson-Darling test reports at 5  
 859 different confidence levels. These results only register interannual variability (one day per year).  
 860 **Bottom row:** The left plot compares the daily temperature anomalies over all of June and July  
 861 subset for 5 different periods (1979–1999, 1981–2010, 1991–2020, 2000–2020, and 1979–2020,  
 862 from left to right). The right plot shows the skewness (red) calculated for temperature data for  
 863 each of the 5 period subsets, along with the *p*-value of the skew test (.1 and .05 significance  
 864 levels indicated). These results register both interannual and intra-annual variability (61 days per  
 865 year over 21- or 30-year periods).

866

867



868 **Fig. S15: Nonstationary-location, stationary-scale GEV fit.** Same as Fig. 4 but for the GEV fit

869 with fixed scale parameter

870

871

ERA5 data

*Does allowing nonstationarity in the location and/or scale parameters improve the GEV model fit? Finding the test statistic  $D > 0$  indicates improvement, with significance tested according to the critical values in the bottom table.*

	Location	Scale
Fit with 2021	D=18.749 ( <b>p&lt;0.001</b> )	D=6.593 ( <b>p&lt;0.025</b> )
Fit without 2021	D=20.837 ( <b>p&lt;0.001</b> )	D=1.231 (p=0.267)

Model data

*Does allowing nonstationarity in the location parameter improve the GEV model fit?*

	Covariate: PNWMST	Covariate: GMST
Prescribed SM	D=3.573 ( <b>p&lt;0.1</b> )	D=0.461 (p>0.1)
Interactive SM	D=13.836 ( <b>p&lt;0.001</b> )	D=2.400 (p>0.1)

Critical values and significance definitions (from 1-d.o.f. Chi-square distribution):

Critical values of D	D=2.706	D=3.841	D=5.024	D=6.635	D=10.828
Significance if critical value exceeded	p<0.1	p<0.05	p<0.025	p<0.01	p<0.001

874 **Table S1: Likelihood Ratio Test.** The Likelihood Ratio Test (from Theorem 2.7 of Coles et al.  
 875 (2001) tests whether adding nonstationarity in parameters improves the GEV model fit. Tables  
 876 show test statistics (D) and significance levels for adding nonstationarity in the location and scale  
 877 parameters for ERA5 data and nonstationarity in the location parameter for model data, with  
 878 different covariates.